Performance Analysis of FAS-Aided NOMA-ISAC: A Backscattering Scenario

Farshad Rostami Ghadi, *Member*, *IEEE*, Kai-Kit Wong, *Fellow*, *IEEE*, F. Javier López-Martínez, *Senior Member*, *IEEE*, Hyundong Shin, *Fellow*, *IEEE*, and Lajos Hanzo, *Life Fellow*, *IEEE*

***Abstract*—This paper investigates a two-user downlink system for integrated sensing and communication (ISAC) in which the two users deploy a fluid antenna system (FAS) and adopt the non-orthogonal multiple access (NOMA) strategy. Specifically, the integrated sensing and backscatter communication (ISABC) model is considered, where a dual-functional base station (BS) serves to communicate the two users and sense a tag's surrounding. In contrast to conventional ISAC, the backscattering tag reflects the signals transmitted by the BS to the NOMA users and enhances their communication performance. Furthermore, the BS extracts environmental information from the same backscatter signal in the sensing stage. Firstly, we derive closed-form expressions for both the cumulative distribution function (CDF) and probability density function (PDF) of the equivalent channel at the users utilizing the moment matching method and the Gaussian copula. Then in the communication stage, we obtain closed-form expressions for both the outage probability and for the corresponding asymptotic expressions in the high signal-to-noise ratio (SNR) regime. Moreover, using numerical integration techniques such as the Gauss-Laguerre quadrature (GLQ), we have series-form expressions for the user ergodic communication rates (ECRs). In addition, we get a closed-form expression for the ergodic sensing rate (ESR) using the Cramér-Rao lower bound (CRLB). Finally, the accuracy of our analytical results is validated numerically, and we confirm the superiority of employing FAS over traditional fixed-position antenna systems in both ISAC and ISABC.**

***Index Terms*—Backscatter, Cramér-Rao bound, ergodic capacity, fluid antenna system, integrated sensing and communication, non-orthogonal multiple access.**

I. Introduction

THE RAPID proliferation of intelligent devices and the fast escalating demand for high-efficiency wireless communication present critical challenges in the next-generation of wireless networks, a.k.a. the sixth generation (6G) [1], [2], [3]. One growing technology, which has become a key use case in 6G, is integrated sensing and communication (ISAC) [4]. ISAC merges sensing and communication (S&C) functionalities into a single framework. Different from conventional frequency-division sensing and communication techniques which require separate frequency bands and dedicated hardware infrastructures for joint S&C, ISAC provides a more efficient solution in terms of spectrum, energy, and hardware usage [5], [6], [7].

Although ISAC is appealing, it makes the provision of S&C functionalities harder, not easier as we are required to squeeze more from what is already limited in the physical layer. As a result, in this context, there is a pressing desire to increase the degrees-of-freedom (DoF) in the physical layer. For decades, multiple-input multiple-output (MIMO) has been responsible for raising the DoF for great benefits if multiple antennas are deployed at both ends. MIMO however comes with expensive radio-frequency (RF) chains and is also subject to strict space constraints. Recently, a promising solution to overcome these issues is to adopt the fluid antenna system (FAS) technology [8], [9] as opposed to a traditional antenna system (TAS). A FAS represents the new form of reconfigurable antennas that enables shape and position flexibility [10]. With FAS, a wireless communication channel can deliver more diversity with less space and less number of RF chains [11], [12], [13], [14], [15]. Recent efforts also studied the use of FAS at both ends of the channel [16]. Channel estimation for FAS has also become an important research problem [17], [18], [19]. In addition, artificial intelligence (AI) techniques are increasingly relevant to the design and optimization of FAS [20], [21]. The emerging movable antenna systems also fall under the category of FAS, specifying the implementation of using stepper motors [22]. Encouraging experimental results have recently been reported to validate the promising performance of FAS [23], [24].

On the other hand, backscatter communication (BC) is rising as a cost-effective technique for ultra-low-power communication technologies [25], [26]. BC exploits passive reflection of existing ambient RF signals to transmit data, thereby eliminating the need for an internal power source for transmission. Hence, BC has great potential to significantly enhance the efficiency and sustainability of wireless networks, facilitating widespread connectivity among a diverse array of Internet-of-Things (IoT) devices and sensors in 6G networks [27]. Moreover, BC has been investigated in NOMA-based systems to enable low-power connectivity and efficient spectrum shar-

The work of F. Rostami Ghadi and K. K. Wong is supported by the Engineering and Physical Sciences Research Council (EPSRC) under Grant EP/W026813/1. The work of F. J. López-Martínez is supported by grant PID2023-149975OB-I00 (COSTUME) funded by MICIU/AEI/10.13039/501100011033, and by ERDF/EU. L. Hanzo would like to acknowledge the financial support of the Engineering and Physical Sciences Research Council (EPSRC) projects Platform for Driving Ultimate Connectivity (TITAN) under Grant EP/X04047X/1 and Grant EP/Y037243/1.

F. Rostami Ghadi is with the Department of Electronic and Electrical Engineering, University College London, WC1E 7JE London, U.K. (e-mail: f.rostamighadi@ucl.ac.uk).

K. K. Wong is with the Department of Electronic and Electrical Engineering, University College London, WC1E 7JE London, U.K., and also with the Department of Electronic Engineering, Kyung Hee University, Yongin-si, Gyeonggi-do 17104, Republic of Korea. (e-mail: kai-kit.wong@ucl.ac.uk).

F. J. López-Martínez is with the Department of Signal Theory, Networking and Communications, Research Centre for Information and Communication Technologies (CITIC-UGR), University of Granada, 18071, Granada, Spain, and also with the Communications and Signal Processing Lab, Telecommunication Research Institute (TELMA), Universidad de Málaga, Málaga, 29010, Spain. (e-mail: fjlm@ugr.es).

Hyundong Shin is with the Department of Electronics and Information Convergence Engineering, Kyung Hee University, Yongin-si, Gyeonggi-do 17104, Republic of Korea. (e-mail: hshin@khu.ac.kr).

L. Hanzo is with the School of Electronics and Computer Science, University of Southampton, Southampton, U.K. (e-mail: lh@ecs.soton.ac.uk).

Corresponding authors: Kai-Kit Wong, Hyundong Shin.

ing [28], [29]. Recent studies have explored the integration of BC with NOMA, demonstrating its potential for enabling simultaneous multi-user access and energy-efficient connectivity [30]. In our proposed FAS-aided NOMA-ISABC system, the backscatter tag serves as a passive reflector that enhances the communication link and supports sensing, which differs from conventional BC systems where the tag actively modulates its own data.

Overall, it is clear that ISAC, FAS and BC can be strategically combined for an efficient solution, which motivates the work of this paper.

A. State-of-the-Art

Some efforts have been undertaken in the context of ISAC, FAS, and BC from various aspects and some of their intersections in recent years. For example, [31] analyzed the diversity order to evaluate the sensing rate (SR) and communication rate (CR) for both downlink and uplink ISAC systems. Also, [32] derived novel expressions for the outage probability (OP), the ergodic CR (ECR), and the SR for ISAC. By extending the results in [31], [32] to a downlink MIMO system for ISAC, the diversity orders and high signal-to-noise ratio (SNR) slopes of the SR and CR were subsequently derived in [33].

Besides, non-orthogonal multiple access (NOMA) has often been considered in the application of ISAC because it expands the capacity region by making better use of the available DoF. Recently in [34], the authors studied a cooperative ISAC network for non-orthogonal downlink transmission, where they characterized the exact and asymptotic OP, the ECR, and the probability of successful sensing detection. Also, the sum of ECR and the signal-to-interference plus noise ratio (SINR) of the sensing signal were maximized. In [35], a dual-functional base station (BS) was considered to serve users in the uplink using NOMA and a beamforming design problem was studied to maximize the weighted sum of CR and the effective sensing power. Later in [36], the impact of successive interference cancellation (SIC) in NOMA-ISAC was investigated. Moreover, using the concept of semi-ISAC under NOMA, [37] obtained analytical expressions for the OP, the ECR, and the ergodic radar estimation information rate. Most recently, the CR and SR for a near-field ISAC system was studied in [38].

On the other hand, there have also been significant research on FAS as mentioned earlier. Some recent efforts have looked into the combination of FAS and NOMA for communication [39], [40] with the latter work also considering wireless power transfer. ISAC using FAS is not well understood nonetheless, with only few recent work beginning to highlight the benefits of FAS for ISAC scenarios. For example, with FAS at the BS serving in the downlink for ISAC, the authors in [41] devised a proximal distance algorithm to solve the multiuser sum-rate maximization problem with a radar sensing constraint to obtain the closed-form beamforming vector, and also an extrapolated projected gradient algorithm to obtain a better antenna location configuration for FAS to enhance the ISAC performance. Most recently, machine learning techniques have also been used to optimize a downlink MIMO network with FAS at the BS for ISAC subjected to a sensing constraint [42]. Further, masked autoencoders were employed to only exploit partial channel state information (CSI) at the BS with great effect.

Relatively speaking, the intersection between BC and other technologies is even less explored. The only work considering both FAS and BC appears to be [43], in which a closed-form expression for the cumulative distribution function (CDF) of the equivalent channel at the FAS-enabled reader was found and the impact of FAS was revealed. On the other hand, the concept of integrated sensing and BC (ISABC) was proposed in [44]. Conventional ISAC attempts to integrate S&C using active devices and passive objects, while ISABC enhances this capability by incorporating backscatter tags. The tags enable passive objects equipped with them to reflect and modulate existing signals from the ISAC system.

Following [44], several important performance metrics such as the probability of detection, linear estimation error, least-squares estimation error, and linear minimum mean-square-error estimation were derived in [45]. Additionally, the authors in [46] optimized beamforming and power allocation within an ISAC system by using backscattering tags in order to enhance both tag detection and user communication subject to a total power constraint. Furthermore, [47] optimized beamforming and tag reflection in an ISABC system to improve S&C rates, while minimizing the BS's power consumption. The authors of [48] proposed leveraging radar clutter as a carrier signal to enable ambient BC, developing novel encoding and decoding schemes to exploit the periodic structure of radar excitation, while also evaluating the trade-offs between transmission rate and error probability. In contrast to [48], the authors in [49] explored a pilot-based approach and introduced a simplified decoding scheme that utilizes constrained regularized least squares, with the associated per-iteration complexity scaling linearly with the data size. In [50], a NOMA-enabled ISABC system is studied, where joint beamforming is optimized to maximize user sum-rate while ensuring tag detection and quality of service (QoS) constraints, using an alternating optimization (AO)-based algorithm under a multi-user setup. Additionally, An rate-splitting multiple access (RSMA)-assisted ISABC system with a full-duplex BS is proposed in [51], where joint optimization of beamforming and reflection coefficients enhances communication efficiency compared to NOMA-assisted ISABC. In summary, however, FAS-aided ISABC has not been studied before. The unique contributions of our work are prominently highlighted in Table I, allowing for an easy comparison with existing studies. The detailed contributions of this paper are also discussed in the following section for clarity.

B. Motivation and Contributions

The beauty of ISAC for simultaneous S&C with lessened hardwares and shared resources, the new DoF enabled by FAS and the great potential of BC in utilizing ambient signals, have motivated us to investigate the synergy between ISAC, FAS, and BC. The synergy of these technologies promises a robust, adaptable, and efficient communication framework ideal for supporting the demanding requirements of next-generation IoT

TABLE I
COMPARISON OF OUR CONTRIBUTIONS TO THE LITERATURE

Works	ISAC	FAS	BC	NOMA	SR	CR	OP
[32], [34], [36], [37]	✓			✓	✓	✓	✓
[38]	✓				✓	✓	
[39]		✓		✓		✓	
[40]		✓					✓
[41]	✓	✓			✓	✓	
[42]	✓	✓				✓	
[43]		✓	✓				✓
[44]	✓		✓		✓	✓	
[45]	✓		✓		✓	✓	
[46]	✓		✓				
[47]	✓		✓		✓	✓	
[50]	✓		✓	✓		✓	
[51]	✓		✓		✓	✓	
Proposed	✓	✓	✓	✓	✓	✓	✓

Table Notation. The proposed work uniquely integrates all listed features (ISAC, FAS, BC, NOMA, SR, CR, and OP), providing a comprehensive approach not found in any of the other reviewed works.

and performance-critical wireless networks [1]. Motivated by the above, we consider an ISABC scenario adopting the NOMA technology, where a backscatter tag serves as the sensing target and the communication users are equipped with FAS. The tag not only provides sensing information to the BS but also contributes path diversity to the FAS-equipped NOMA users via passive signal reflection, without modulating its own data[2].

Specifically, our main contributions are as follows:

- First of all, we characterize both the CDF and probability density function (PDF) of the ISABC equivalent channel at the FAS-equipped NOMA users, exploiting the moment matching technique and copula theory.
- Then, in the communication stage, we derive the closed-form expressions for the OP, as well as their respective asymptotic expressions in the high SNR regime. Besides, we provide integral-form expressions of the ECR and approximate them using numerical integration techniques such as the Gauss-Laguerre quadrature (GLQ).
- Afterwards, we obtain a closed-form expression for the ergodic SR (ESR) in the sensing stage, using the Cramér-Rao lower bound (CRLB).
- Finally, we evaluate the accuracy of our theoretical results and compare them to several benchmarks. Our findings indicate enhanced overall performance, demonstrating the superiority of FAS over TAS in both ISAC and ISABC scenarios. Additionally, we provide an accurate trade-off between SR and CR to gain further insights into the performance of the proposed system.

[1]The theoretical model presented in this paper highlights the potential of FAS-aided ISAC in BC scenarios, but practical deployment faces challenges such as hardware complexity, power consumption, and scalability for managing massive connectivity. Reconfiguring antennas in real-time requires efficient integration with existing systems, a challenge addressed by works like [23], [24]. While reconfiguration increases power consumption, studies such as [40] show that it can be managed without significantly impacting power budgets. Additionally, the scalability of FAS to handle large-scale scenarios was demonstrated in [52], [53], which offer solutions for supporting massive connectivity and efficient communication in high-density environments.

[2]This passive reflection, consistent with ISABC [44], enhances the user channels by introducing path diversity. The tag does not encode or transmit its own data but acts as a non-information-bearing reflector, supporting communication and sensing without conventional backscatter modulation.

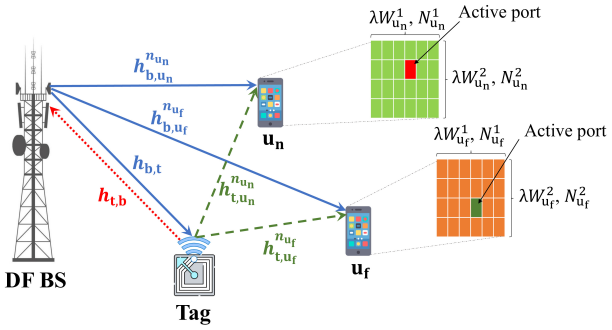

Fig. 1. The system model of ISABC with two FAS-aided users and one backscatter tag.

C. Paper Organization

The remainder of this paper is organized as follows. Section II introduces the system model of ISABC for both the S&C stages. The statistical characteristics of the equivalent channel, including communication performance such as OP and ECR analysis, and sensing performance such as ESR analysis, are presented in Section III. Section IV provides the numerical results, and finally, Section V concludes this paper.

D. Mathematical Notations

Throughout, we use boldface upper and lower case letters $\mathbf{X}$ and $\mathbf{x}$ for matrices and column vectors, respectively. $\mathbb{E}[\cdot]$ and $\mathrm{Var}[\cdot]$ denote the mean and variance operators, respectively. Moreover, $(\cdot)^T$, $(\cdot)^{-1}$, $|\cdot|$, and $\det(\cdot)$ stand for the transpose, inverse, magnitude, and determinant, respectively.

II. System and Channel Models

A. System Model

As shown in Fig. 1, we consider a wireless communication system, where a dual-functional BS communicates with a pair of NOMA users, i.e., one near (strong) user $\mathrm{u_n}$ and one far (weak) user $\mathrm{u_f}$, while simultaneously broadcasts a sensing waveform to sense a single fixed-position antenna tag.[3] Both users $\mathrm{u_n}$ and $\mathrm{u_f}$ are equipped with a planar FAS, while the BS includes two fixed-position antennas, one for transmitting and another for receiving signals. In this regard, we assume that the BS antennas are spatially well separated in order to cancel the self-interference. The FAS-equipped users $i \in \{\mathrm{u_n}, \mathrm{u_f}\}$, consist of a grid structure with N_i^l ports that

[3]This model can be extended to more general scenarios such as high-mobility environments and multiuser or multi-tag systems. In high-mobility scenarios, accounting for Doppler effects and rapid channel variation would require adaptive FAS and NOMA strategies to maintain communication and sensing accuracy. Expanding to multiuser or multi-tag setups could enhance scalability and coverage, though it would necessitate advanced interference management and resource allocation techniques. These scenarios are potential directions for future work, offering opportunities to broaden robustness and scalability of ISABC systems in complex and dynamic environments.

TABLE II
SUMMARY OF KEY NOTATIONS AND PARAMETERS

Symbol	Description
$h_{\mathrm{b},i}^{n_i}$	Channel from BS to FAS user i
$h_{\mathrm{b,t}}$	Channel from BS to the tag
$h_{\mathrm{t,b}}$	Channel from the tag to BS
$h_{\mathrm{t},i}^{n_i}$	Backscatter channel from tag to FAS user i
$g_{\mathrm{fas},i}$	Equivalent channel gain at FAS user i
$g_{\mathrm{eq},i}$	Overall equivalent channel power gain
P_{b}	Transmit power
p_i	power allocation factor of user i
N_i	Number of ports at FAS for user i
W_i	Normalized spatial size of the FAS at user i
ζ	Reflection coefficient of the tag
γ_i	SNR at user i
$\overline{\gamma}$	Average transmit SNR
$\hat{\gamma}_{\mathrm{th}}$	SNR threshold
α	Path-loss exponent
β	Duty cycle of the radar
γ_{echo}	Echo SNR
μ_χ	Splitting factor for communication and sensing
$\mathcal{F}(\cdot)$	Mapping function from 2D port indices to 1D index
η	Dependence parameter of the Gaussian copula
ρ_{s}	Spearman's rank correlation coefficient
τ_{s}	Kendall's rank correlation coefficient
$f_{g_{\mathrm{fas},i}}(\cdot)$	PDF of the FAS channel gain
$F_{g_{\mathrm{fas},i}}(\cdot)$	CDF of the FAS channel gain
T	Pulse duration of the radar
σ^2	Noise power
$d_{\mathrm{b},i}$	Distance between BS and user i
$d_{\mathrm{b,t}}$	Distance between BS and the tag
$d_{\mathrm{t},i}$	Distance between the tag and user i
ϱ_i	Covariance between two arbitrary ports at user i
$\mathbf{R}_i$	Spatial correlation matrix

are uniformly distributed along a linear space of length $W_i^l\lambda$ for $l \in \{1,2\}$, i.e., $N_i = N_i^1 \times N_i^2$ and $W_i = W_i^1\lambda \times W_i^2\lambda$. Additionally, a bijective mapping function $\mathcal{F}: (n_1^i, n_2^i) \mapsto n_i$ is used for conveniently transforming the two-dimensional (2D) spatial indices of the FAS ports into a one-dimensional (1D) linear index. Its inverse, $\mathcal{F}^{-1}(n_i) = (n_1^i, n_2^i)$, allows the retrieval of the original 2D coordinates. This row-major indexing simplifies the representation of the signal model and facilitates the optimal port selection process in performance analysis. Under this model, the BS transmits a signal $x(t)$ at the t-th time slot for both communication and sensing.[4] The total power has to be split into two parts according to $\mu_\chi \in [0,1]$ for $\chi \in \{\mathrm{c},\mathrm{s}\}$, with one part for sensing and the other for communications, i.e., $\mu_{\mathrm{c}} + \mu_{\mathrm{s}} = 1$, in which the subscripts 'c' and 's' specify the splitting factor for communications and sensing, respectively.

B. Signal and Channel Models

1) Communication stage: The received signal at the n_i-th port of user i via the tag at the t-th time slot is given by

$$y_i^{n_i}(t) = \sqrt{P_{\mathrm{b}}\mu_{\mathrm{c}}}h_{\mathrm{eq},i}^{n_i}\left[\sqrt{p_{\mathrm{u_n}}}x_{\mathrm{u_n}}(t) + \sqrt{p_{\mathrm{u_f}}}x_{\mathrm{u_f}}(t)\right] + z_i^{n_i}(t), \tag{1}$$

in which P_{b} denotes the transmit power and p_i is the power allocation factor satisfying $p_{\mathrm{u_n}} + p_{\mathrm{u_f}} = 1$. Moreover, $x_{\mathrm{u_n}}(t)$ and $x_{\mathrm{u_f}}(t)$ represent the symbols transmitted to the near user $\mathrm{u_n}$ and the far user $\mathrm{u_f}$, respectively, with $\mathbb{E}\left[|x_i(t)|^2\right] = 1$ for $i \in \{\mathrm{u_n}, \mathrm{u_f}\}$. The term $h_{\mathrm{eq},i}^{n_i} = d_{\mathrm{b},i}^{-\alpha}h_{\mathrm{b},i}^{n_i} + \zeta d_{\mathrm{b,t}}^{-\alpha}d_{\mathrm{t},i}^{-\alpha}h_{\mathrm{b,t}}h_{\mathrm{t},i}^{n_i}$ represents the equivalent channel (i.e., the sum of the direct and effective backscatter channels) at the n_i-th port of user i, where $\zeta \in [0,1]$ is the tag's reflection coefficient, $h_{\mathrm{b},i}^{n_i}$ defines the channel coefficient between the BS and the n_i-th port at the FAS-equipped user i, $h_{\mathrm{b,t}}$ is the channel coefficient between the BS and the tag, and $h_{\mathrm{t},i}^{n_i}$ is the channel coefficient between the tag and the n_i-th port of user i. It is important to note that the backscatter tag in our model does not inject independent data but passively reflects the BS's signal with a fixed reflection coefficient ζ. This setup follows the ISABC paradigm of [44], where the tag serves as a passive reflector enhancing communication and sensing without active data modulation. Additionally, $d_{\mathrm{b},i}$, $d_{\mathrm{b,t}}$, and $d_{\mathrm{t},i}$ represent, respectively, the distances from the BS to user i, the BS to the tag, and the tag to user i. Moreover, $\alpha > 2$ denotes the path-loss exponent. Also, $z_i^{n_i}(t) \sim \mathcal{CN}\left(0,\sigma^2\right)$ defines the additive white Gaussian noise (AWGN) with zero mean and variance σ^2 at the n_i-th port of user i.

Remark 1. *In contrast to conventional backscatter communication, where the tag modulates and transmits its own data [25], [26], the tag in our model, as seen in (1), acts solely as a passive reflector. It reflects the incident signal from the BS to the users without embedding any information, consistent with the ISABC framework [44], [45]. Thus, while the tag does not contribute independent data, its presence improves communication by providing additional propagation paths and enhances sensing via radar-like echoes.*

2) Sensing stage: Given that the backscattered signal at the tag is received by both users and the BS, the BS utilizes this signal to extract environmental information. In this context, we assume that the BS knows the type of pulse sent to the tag and has previously gathered observations to estimate the predicted range of the tag's position. If pulses are consistently transmitted to the tag at a fixed frequency, the BS can calculate the predicted echo using the prior observations. It is worth noting that uncertainty in the positioning is directly related to time delay fluctuations in radar systems [54]. Therefore, under these assumptions, the time delay fluctuation t_{df} follows a Gaussian distribution[5] with the variance of $\sigma_{t_{\mathrm{df}}}^2 = \mathbb{E}\left[|t_{\mathrm{df}} - t_{\mathrm{pre}}|^2\right]$, in which t_{pre} is the predicted value of t_{df}. As a result, the average power level of the echo signal, considering the uncertainty in the positioning decision, is formulated as [54]

$$\sigma_{\mathrm{echo}}^2 = \mathbb{E}\left[|x(t - t_{\mathrm{df}}) - x(t - t_{\mathrm{pre}})|^2\right] \approx \frac{\pi^2}{3}\sigma_{t_{\mathrm{df}}}^2. \tag{2}$$

As such, by transmitting the signal $x(t)$ to sense the tag surrounding environment, the BS receives the following reflected

[4]From a sensing perspective, $x(t)$ represents the radar snapshot transmitted at the t-th time slot, and for communications, it is the t-th data symbol [31].

[5]This assumption is commonly applied in radar systems, where time delay fluctuations arise from random variations such as noise and propagation uncertainties, which result from multiple independent sources [54]. It is consistent with established information-theoretic models for radar-based sensing, particularly in scenarios where small, independent variations in signal propagation times accumulate, leading to a distribution that can be accurately described by the central limit theorem.

echo signal at its receive antenna, i.e.,

$$y_{\mathrm{b}}(t)=\sqrt{P_{\mathrm{b}}\mu_{\mathrm{s}}\zeta}h_{\mathrm{tsr,t}}\left[x\left(t-t_{\mathrm{df}}\right)-x\left(t-t_{\mathrm{pre}}\right)\right]+z_{\mathrm{b}}(t), \tag{3}$$

in which $z_{\mathrm{b}}(t)\sim\mathcal{CN}\left(0,\sigma^2\right)$ is the AWGN at the BS. Additionally, $h_{\mathrm{tsr,t}}=h_{\mathrm{t,b}}h_{\mathrm{b,t}}$ denotes the tag sensing response (TSR) that consists of both the channel from the BS to the tag and that from the tag to the BS.

Furthermore, the ports at the FAS of each user can freely switch to a favourable position but they are in close proximity to each other, thus exhibiting spatial correlation in the channel coefficients. Assuming all links undergo Rayleigh fading channels[6], the covariance between two arbitrary ports n_i and $\tilde{n}_i$ at each user i in a three-dimensional (3D) environment with rich scattering can be defined as [16]

$$\varrho_i=j_0\left(2\pi\sqrt{\left(\frac{n_i^1-\tilde{n}_i^1}{N_i^1-1}W_i^1\right)^2+\left(\frac{n_i^2-\tilde{n}_i^2}{N_i^2-1}W_i^2\right)^2}\right), \tag{4}$$

where $\tilde{n}_i=\mathcal{F}^{-1}\left(\tilde{n}_i^1,\tilde{n}_i^2\right)$ for $\tilde{n}_i^l\in\left\{1,\ldots,N_i^l\right\}$ and $j_0(.)$ is the zero-order spherical Bessel function of the first kind.

C. SINR Characterization

Given that NOMA is used for the users, the optimal decoding technique involves implementing SIC according to the near FAS-equipped user i. To that end, the near user first decodes the signal transmitted to the far user treating its own signal as noise. Additionally, each FAS-equipped user can activate only a single port at a time, so the port that maximizes the equivalent channel gain is selected. Therefore, for user i, this optimal port index is denoted as n_i^*, which is given by

$$n_i^*=\arg\max_{n}\left\{\left|h_{\mathrm{eq},i}^{n_i}\right|^2\right\}, \tag{5}$$

where $g_{\mathrm{eq},i}^{n_i}=\left|h_{\mathrm{eq},i}^{n_i}\right|^2$ is the equivalent channel gain. Thereby, all SINR expressions are evaluated at this selected port. Moreover, the channel gain at the FAS-equipped user i is simply the equivalent channel gain at this best port, which we denote as

$$g_{\mathrm{fas},i}=\left|h_{\mathrm{eq},i}^{n_i^*}\right|^2. \tag{6}$$

Therefore, assuming that only the optimal port that maximizes the received SINR at the FAS-equipped users is activated, the SINR of the SIC process can be expressed as

$$\gamma_{\mathrm{sic}}=\frac{\overline{\gamma}p_{\mathrm{u_f}}\mu_{\mathrm{c}}\left|h_{\mathrm{eq,u_n}}^{n_{\mathrm{u_n}}^*}\right|^2}{\overline{\gamma}p_{\mathrm{u_n}}\mu_{\mathrm{c}}\left|h_{\mathrm{eq,u_n}}^{n_{\mathrm{u_n}}^*}\right|^2+1}, \tag{7}$$

in which $\overline{\gamma}=\frac{P_{\mathrm{b}}}{\sigma^2}$ denotes the average SNR. Then, $\mathrm{u_n}$ removes the message of $\mathrm{u_f}$ from its received signal and decodes its own required information. As a consequence, the received SNR at the FAS-equipped user $\mathrm{u_n}$ is expressed as

$$\gamma_{\mathrm{u_n}}=\overline{\gamma}p_{\mathrm{u_n}}\mu_{\mathrm{c}}\left|h_{\mathrm{eq,u_n}}^{n_{\mathrm{u_n}}^*}\right|^2. \tag{8}$$

Simultaneously, the far user $\mathrm{u_f}$ directly decodes its own signal but lacks the capability to filter out the signal from the near user $\mathrm{u_n}$ within the combined transmitted message. This implies that the far FAS-equipped user $\mathrm{u_f}$ must decode its signal directly by treating interference as noise. Thus, the received SINR at the far FAS-equipped user $\mathrm{u_f}$ is given by

$$\gamma_{\mathrm{u_f}}=\frac{\overline{\gamma}p_{\mathrm{u_f}}\mu_{\mathrm{c}}\left|h_{\mathrm{eq,u_f}}^{n_{\mathrm{u_f}}^*}\right|^2}{\overline{\gamma}p_{\mathrm{u_n}}\mu_{\mathrm{c}}\left|h_{\mathrm{eq,u_f}}^{n_{\mathrm{u_f}}^*}\right|^2+1}. \tag{9}$$

III. Performance Analysis

In this section, we analyze the performance of the FAS-aided NOMA-ISAC system in both communication and sensing stages. While data-driven and optimization-based approaches are increasingly used in modern ISAC system design, closed-form performance analysis remains highly valuable. It enables lightweight, real-time computation in resource-constrained IoT deployments and provides theoretical insights into how key parameters influence performance. These expressions also serve as benchmarks for validating machine learning or numerical optimization techniques. We begin by deriving the CDF and PDF of the equivalent channel at the FAS-equipped NOMA users, which helps in statistically characterizing the channel's behavior under various environmental conditions. This characterization is essential for assessing signal reliability in real-world scenarios.

In the communication stage, we derive compact analytical expressions for the OP and its asymptotic behavior. These expressions provide insights into the likelihood of transmission failures due to insufficient SNR, which is critical for ensuring reliable communication. We also obtain the ECR, representing the long-term average data rate under realistic, fluctuating channel conditions. ECR offers a measure of the system's efficiency and robustness in fast-changing ISAC environments where maintaining consistent communication performance is essential for both data and sensing accuracy.

Finally, in the sensing stage, we derive a closed-form expression for the ESR, capturing the system's ability to track environmental changes over time. ESR provides insight into the effectiveness of the ISAC system's sensing functionality, ensuring that it can adapt responsively in complex environments. Together, these metrics enable a comprehensive evaluation of the system's performance across both communication and sensing functionalities.

A. Statistical Characteristics

Given (1) and (6), the equivalent channel at both users over the communication stage includes the maximum of N_i correlated random variables (RVs), each of which includes the sum of two independent RVs, where one follows a Rayleigh

[6]While Rayleigh fading is used in this paper for its analytical simplicity and relevance in non-line-of-sight (NLoS) environments such as indoor IoT and passive tag settings, the proposed framework including the copula-based modeling and Gamma approximation can be extended to more general fading models like Nakagami-m. This allows capturing a wider range of channel conditions, but this is left for future investigation.

distribution and the other one is the product of two independent exponentially-distributed RVs [55]. We exploit a flexible statistical approach in the statistics theory called Sklar's theorem, which can generate the joint CDF of many arbitrarily correlated RVs, e.g., N_i, beyond linear dependency by only using the marginal distribution of each RV and a specific function. For this purpose, let $\mathbf{s} = [S_1, \ldots, S_d]$ be a vector of d arbitrary correlated RVs having the univariate marginal CDF $F_{S_j}(s_j)$ and joint multivariate CDF $F_{S_1,\ldots,S_d}(s_1, \ldots, s_d)$ for $j \in \{1, \ldots, d\}$, respectively. Then, in the extended real line domain $\overline{\mathbb{R}}$, the corresponding joint CDF is given by [56]

$$F_{S_1,\ldots S_N}(s_1, \ldots, s_d) = C\left(F_{S_1}(s_1), \ldots, F_{S_d}(s_d); \vartheta\right), \quad (10)$$

in which $C(\cdot) : [0,1]^d \to [0,1]$ denotes the copula function that is a joint CDF of d random vectors on the unit cube $[0,1]^d$ with uniform marginal distributions, i.e., [56]

$$C(u_1, \ldots u_d; \vartheta) = \Pr\left(U_1 \leq u_1, \ldots, U_d \leq u_d\right), \quad (11)$$

where $u_j = F_{S_j}(s_j)$ and ϑ denotes the copula dependence parameter, which measures the structure of dependency between two arbitrarily correlated RVs. Therefore, by choosing an appropriate copula function, the respective joint CDF can be derived. In this regard, we adopt a multivariate Gaussian copula to model the spatial correlation across FAS ports, due to its analytical tractability and compatibility with standard fading distributions [57]. This choice captures symmetric dependence between ports and enables closed-form derivations in later sections. While alternative copulas like the Archimedean Copulas may model asymmetric or tail-dependent behavior, they introduce significant analytical complexity and are more suited for measurement-driven or non-symmetric scenarios. In particular, the correlation coefficient of Jake's model is accurately approximated by the dependence parameter of the Gaussian copula for any arbitrarily correlated fading channels[7]. The multivariate Gaussian copula associated with the correlation matrix $\mathbf{R}$ can be found by

$$C_{\mathrm{G}}(u_1, \ldots, u_d; \eta) = \mathbf{\Phi}_{\mathbf{R}}\left(\varphi^{-1}(u_1), \ldots, \varphi^{-1}(u_d); \eta\right), \quad (12)$$

in which $\varphi^{-1}(u_q) = \sqrt{2}\mathrm{erf}^{-1}(2u_q - 1)$ defines the inverse CDF (quantile function) of the standard normal distribution, with $\mathrm{erf}^{-1}(\cdot)$ denoting the inverse of the error function $\mathrm{erf}(s) = \frac{2}{\sqrt{\pi}}\int_0^s \mathrm{e}^{-t^2}\mathrm{d}t$. The term $\mathbf{\Phi}_{\mathbf{R}}(\cdot)$ is the joint CDF of the multivariate normal distribution with a zero mean vector and a correlation matrix $\mathbf{R}$. Also, the term $\eta \in (-1, 1)$ denotes the dependence parameter of the Gaussian copula, which measures and controls the degree of dependence between correlated RVs. Moreover, using the chain rule, the density function c_{G} of the Gaussian copula is expressed as [57]

$$c_{\mathrm{G}}(u_1, \ldots, u_d; \eta) = \frac{\exp\left(-\frac{1}{2}\left(\boldsymbol{\varphi}^{-1}\right)^T\left(\mathbf{R}^{-1} - \mathbf{I}\right)\boldsymbol{\varphi}^{-1}\right)}{\sqrt{\det(\mathbf{R})}}, \quad (13)$$

where $\boldsymbol{\varphi}^{-1}$ denotes a vector containing the quantile function of the standard normal distribution $\varphi^{-1}(u_j)$, $\det(\mathbf{R})$ is the determinant of $\mathbf{R}$, and $\mathbf{I}$ is the identity matrix.

Theorem 1. *The CDF of the channel gain $g_{\mathrm{fas},i}$ at the FAS-equipped NOMA user i under correlated Rayleigh fading is given by (14) (see top of this page), where $\Upsilon(x, y)$ is the lower incomplete gamma function, $\Gamma(x)$ is the gamma function,*

$$\varkappa_i = \frac{d_{\mathrm{b},i}^{-2\alpha}\overline{a}^2 + 3\left(\zeta d_{\mathrm{b,t}}^{-\alpha} d_{\mathrm{t},i}^{-\alpha}\overline{b}\overline{c}\right)^2}{d_{\mathrm{b},i}^{-\alpha}\overline{a} + \zeta d_{\mathrm{b,t}}^{-\alpha} d_{\mathrm{t},i}^{-\alpha}\overline{b}\overline{c}} \quad (15)$$

and

$$\varpi_i = \frac{\left(d_{\mathrm{b},i}^{-\alpha}\overline{a} + \zeta d_{\mathrm{b,t}}^{-\alpha} d_{\mathrm{t},i}^{-\alpha}\overline{b}\overline{c}\right)^2}{d_{\mathrm{b},i}^{-2\alpha}\overline{a}^2 + 3\left(\zeta d_{\mathrm{b,t}}^{-\alpha} d_{\mathrm{t},i}^{-\alpha}\overline{b}\overline{c}\right)^2}, \quad (16)$$

where $\overline{a} = \mathbb{E}\left[g_{\mathrm{b},i}^{n_i}\right]$, $\overline{b} = \mathbb{E}\left[g_{\mathrm{b,t}}\right]$, and $\overline{c} = \mathbb{E}\left[g_{\mathrm{t},i}^{n_i}\right]$. Moreover, the term $\mathbf{\Phi}_{\mathbf{R}_i}(\cdot)$ represents the joint CDF of the multivariate normal distribution with zero mean vector and the following correlation matrix

$$\mathbf{R}_i = \begin{bmatrix} 1 & \eta_{1,2}^i & \cdots & \eta_{1,N_i}^i \\ \eta_{2,1}^i & 1 & \cdots & \eta_{2,N_i}^i \\ \vdots & \vdots & \ddots & \vdots \\ \eta_{N_i,1}^i & \eta_{N_i,2}^i & \cdots & 1 \end{bmatrix}. \quad (17)$$

Proof. See Appendix A. □

The expression in (14) provides a powerful tool for statistically characterizing the equivalent channel behavior at the FAS-equipped users. This CDF not only simplifies the analysis of the SNR/SINR statistical distribution but also allows for precise predictions of system reliability, as it can be used to compute the OP and communication rate metrics.

Theorem 2. *The PDF of the channel gain $g_{\mathrm{fas},i}$ at the FAS-equipped NOMA user i under correlated Rayleigh fading is given by (18) (see top of next page), in which $\psi(x) = \frac{1}{\sqrt{2\pi}}\mathrm{e}^{-\frac{x^2}{2}}$ is the standard normal PDF, and*

$$\boldsymbol{\varphi}^{-1}_{g_{\mathrm{eq},i}^{N_i}} = \left[\sqrt{2}\mathrm{erf}^{-1}\left(\frac{2}{\Gamma(\varkappa_i)}\Upsilon\left(\varkappa_i, \frac{g_{\mathrm{fas}}}{\varpi_i}\right) - 1\right), \ldots, \sqrt{2}\mathrm{erf}^{-1}\left(\frac{2}{\Gamma(\varkappa_i)}\Upsilon\left(\varkappa_i, \frac{g_{\mathrm{fas}}}{\varpi_i}\right) - 1\right)\right].$$

Proof. See Appendix B. □

Similarly, (18) is crucial for calculating the ECR of the FAS-equipped users in the proposed ISABC system, as it allows integration over all possible channel states to capture average performance accurately. By incorporating this PDF, the ECR

[7]The use of η_i in the Gaussian copula correlation matrix is not arbitrary. As shown in [57], it accurately approximates the physical correlation coefficient ϱ_i derived from Jakes' model. This approximation was validated through analytical expressions involving rank correlation metrics, e.g., Spearman's ρ_{s} or Kendall's τ_{k}, and further confirmed by scatterplot comparisons between the Gaussian copula model and the classical Jakes model.

This article has been accepted for publication in IEEE Internet of Things Journal. This is the author's version which has not been fully edited and content may change prior to final publication. Citation information: DOI 10.1109/JIOT.2025.3612478

$$F_{\text{fas},i}\left(g_{\text{fas}}\right)=\Phi_{\mathbf{R}_i}\left(\sqrt{2}\text{erf}^{-1}\left(\frac{2}{\Gamma\left(\varkappa_i\right)}\Upsilon\left(\varkappa_i,\frac{g_{\text{fas}}}{\varpi_i}\right)-1\right),\ldots,\sqrt{2}\text{erf}^{-1}\left(\frac{2}{\Gamma\left(\varkappa_i\right)}\Upsilon\left(\varkappa_i,\frac{g_{\text{fas}}}{\varpi_i}\right)-1\right);\eta_i\right) \tag{14}$$

$$f_{\text{fas},i}\left(g_{\text{fas}}\right)=\sum_{n_i=1}^{N_i}\frac{\partial\Phi_{\mathbf{R}_i}\left(\boldsymbol{\varphi}_{g_{\text{eq},i}^{N_i}}^{-1}\right)}{\partial\varphi^{-1}\left(F_{g_{\text{eq},i}^{n_i}}\left(g_{\text{fas}}\right)\right)}\frac{f_{g_{\text{eq},i}^{n_i}}\left(g_{\text{fas}}\right)}{\psi\left(\varphi^{-1}\left(F_{g_{\text{eq},i}^{n_i}}\left(g_{\text{fas}}\right)\right)\right)} \tag{18}$$

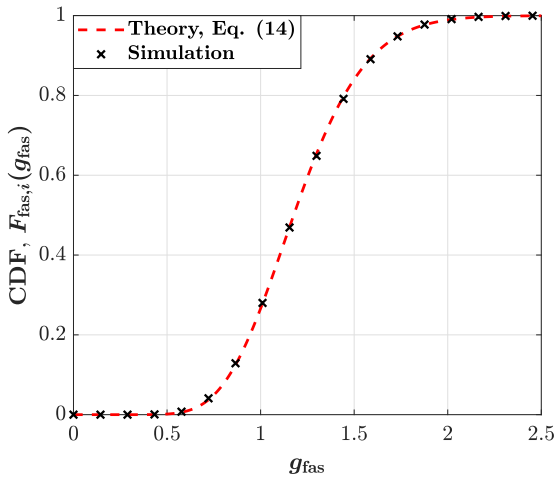

Fig. 2. CDF of the equivalent FAS channel gain $g_{\text{fas},i}$: Comparison between the analytical gamma approximation (Eq. (14)) and Monte Carlo simulation.

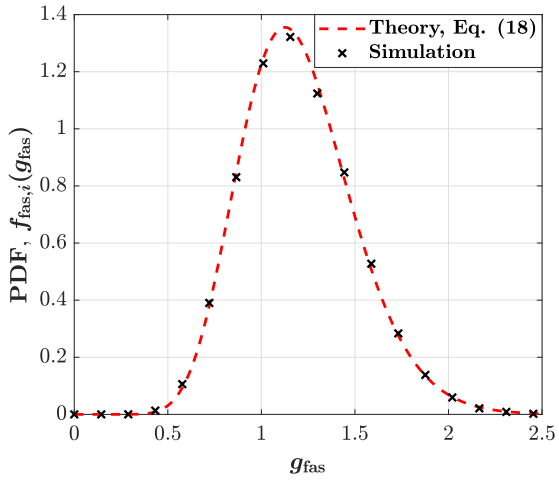

Fig. 3. PDF of the equivalent FAS channel gain $g_{\text{fas},i}$: Comparison between the analytical gamma approximation (Eq. (18)) and Monte Carlo simulation.

calculation fully accounts for channel gain fluctuations, including spatial correlations across the FAS ports, leading to a realistic measure of the system efficiency.

The gamma distribution used to approximate the equivalent FAS channel gain is motivated by its analytical tractability and its ability to accurately match the first two moments of the underlying maximum-based distribution, even under spatially correlated fading modeled via a Gaussian copula. To validate this approximation, Figs. 2 and 3 illustrate the empirical CDF and PDF of the equivalent FAS gain based on Monte Carlo simulations, alongside the corresponding gamma expressions derived via moment matching. The close agreement confirms that the approximation provides a statistically reliable and practically effective model for composite channel behavior, which underpins the accuracy of the closed-form expressions derived for OP, ECR, and ESR. While the exact distribution is analytically intractable due to the complex correlation structure, the gamma approximation strikes a balance between realism and mathematical tractability.

B. Communication Performance

1) OP Analysis: OP is a key performance metric to assess wireless communication systems, which is defined as the probability that the instantaneous SNR γ is below the SNR threshold γ_{th}, i.e., $P_{\text{out}}=\Pr\left(\gamma\leq\gamma_{\text{th}}\right)$.

Theorem 3. *The OP of the near FAS-equipped user* u_n *over the considered FAS-aided ISABC is given by* (19) *(see top of next page), in which*

$$\begin{cases}\tilde{\gamma}_{\text{sic}}=\dfrac{\hat{\gamma}_{\text{sic}}}{\overline{\gamma}\mu_{\text{c}}\left(p_{\text{u}_\text{f}}-\hat{\gamma}_{\text{sic}}p_{\text{u}_\text{n}}\right)},\\ \tilde{\gamma}_{\text{u}_\text{n}}=\dfrac{\hat{\gamma}_{\text{u}_\text{n}}}{\overline{\gamma}\mu_{\text{c}}p_{\text{u}_\text{n}}},\end{cases} \tag{20}$$

where $\hat{\gamma}_{\text{sic}}$ *and* $\hat{\gamma}_{\text{u}_\text{n}}$ *are the corresponding SINR thresholds.*

Proof. OP arises for the near user u_n when it fails to decode its own signal, the far user's signal, or both. Thus, by definition, the OP for u_n can be mathematically expressed as

$$P_{\text{out},\text{u}_\text{n}}=1-\Pr\left(\gamma_{\text{sic}}>\hat{\gamma}_{\text{sic}},\gamma_{\text{u}_\text{n}}>\hat{\gamma}_{\text{u}_\text{n}}\right), \tag{21}$$

in which $\hat{\gamma}_{\text{sic}}$ is the SINR threshold of γ_{sic} and $\hat{\gamma}_{\text{u}_\text{n}}$ denotes the SNR threshold of $\gamma_{\text{u}_\text{n}}$. Given that the OP in the NOMA scenario is mainly affected by the power allocation factors, $P_{\text{out},\text{u}_\text{n}}$ becomes 1 when $p_{\text{u}_\text{f}}\leq\hat{\gamma}_{\text{sic}}p_{\text{u}_\text{n}}$. Therefore, for the case that $p_{\text{u}_\text{f}}>\hat{\gamma}_{\text{sic}}p_{\text{u}_\text{n}}$, the OP can be found as

$$P_{\text{out},\text{u}_\text{n}}$$

$$\overset{(a)}{=}1-\Pr\left(\frac{\overline{\gamma}p_{\text{u}_\text{f}}\mu_{\text{c}}g_{\text{fas},\text{u}_\text{n}}}{\overline{\gamma}p_{\text{u}_\text{n}}\mu_{\text{c}}g_{\text{fas},\text{u}_\text{n}}+1}>\hat{\gamma}_{\text{sic}},\overline{\gamma}p_{\text{u}_\text{n}}\mu_{\text{c}}g_{\text{fas},\text{u}_\text{n}}>\hat{\gamma}_{\text{u}_\text{n}}\right) \tag{22}$$

$$=1-\Pr\left(g_{\text{fas},\text{u}_\text{n}}>\frac{\hat{\gamma}_{\text{sic}}}{\overline{\gamma}\mu_{\text{c}}\left(p_{\text{u}_\text{f}}-\hat{\gamma}_{\text{sic}}p_{\text{u}_\text{n}}\right)},g_{\text{fas},\text{u}_\text{n}}>\frac{\hat{\gamma}_{\text{u}_\text{n}}}{\overline{\gamma}\mu_{\text{c}}p_{\text{u}_\text{n}}}\right) \tag{23}$$

$$=1-\Pr\left(g_{\text{fas},\text{u}_\text{n}}>\max\left\{\tilde{\gamma}_{\text{sic}},\tilde{\gamma}_{\text{u}_\text{n}}\right\}\right) \tag{24}$$

$$=F_{g_{\text{fas},\text{u}_\text{n}}}\left(\tilde{\gamma}_{\max}\right) \tag{25}$$

This article has been accepted for publication in IEEE Internet of Things Journal. This is the author's version which has not been fully edited and content may change prior to final publication. Citation information: DOI 10.1109/JIOT.2025.3612478

$$P_{\text{out},\mathrm{u_n}} = \Phi_{\mathbf{R}_{\mathrm{u_n}}}\left(\sqrt{2}\text{erf}^{-1}\left(\frac{2}{\Gamma\left(\varkappa_{\mathrm{u_n}}\right)}\Upsilon\left(\varkappa_{\mathrm{u_n}}, \frac{\tilde{\gamma}_{\max}}{\varpi_{\mathrm{u_n}}}\right) - 1\right), \ldots, \sqrt{2}\text{erf}^{-1}\left(\frac{2}{\Gamma\left(\varkappa_{\mathrm{u_n}}\right)}\Upsilon\left(\varkappa_{\mathrm{u_n}}, \frac{\tilde{\gamma}_{\max}}{\varpi_{\mathrm{u_n}}}\right) - 1\right); \eta_{\mathrm{u_n}}\right) \tag{19}$$

$$P_{\text{out},\mathrm{u_f}} = \Phi_{\mathbf{R}_{\mathrm{u_f}}}\left(\sqrt{2}\text{erf}^{-1}\left(\frac{2}{\Gamma\left(\varkappa_{\mathrm{u_f}}\right)}\Upsilon\left(\varkappa_{\mathrm{u_f}}, \frac{\tilde{\gamma}_{\mathrm{u_f}}}{\varpi_{\mathrm{u_f}}}\right) - 1\right), \ldots, \sqrt{2}\text{erf}^{-1}\left(\frac{2}{\Gamma\left(\varkappa_{\mathrm{u_f}}\right)}\Upsilon\left(\varkappa_{\mathrm{u_f}}, \frac{\tilde{\gamma}_{\mathrm{u_f}}}{\varpi_{\mathrm{u_f}}}\right) - 1\right); \eta_{\mathrm{u_f}}\right) \tag{26}$$

$$P^{\infty}_{\text{out},\mathrm{u_n}} = \Phi_{\mathbf{R}_{\mathrm{u_n}}}\left(\sqrt{2}\text{erf}^{-1}\left(\frac{2\tilde{\gamma}_{\max}^{\varkappa_{\mathrm{u_n}}}}{\Gamma\left(\varkappa_{\mathrm{u_n}}\right)\varkappa_{\mathrm{u_n}}\varpi_{\mathrm{u_n}}^{\varkappa_{\mathrm{u_n}}}} - 1\right), \ldots, \sqrt{2}\text{erf}^{-1}\left(\frac{2\tilde{\gamma}_{\max}^{\varkappa_{\mathrm{u_n}}}}{\Gamma\left(\varkappa_{\mathrm{u_n}}\right)\varkappa_{\mathrm{u_n}}\varpi_{\mathrm{u_n}}^{\varkappa_{\mathrm{u_n}}}} - 1\right); \eta_{\mathrm{u_n}}\right) \tag{32}$$

$$P^{\infty}_{\text{out},\mathrm{u_f}} = \Phi_{\mathbf{R}_{\mathrm{u_f}}}\left(\sqrt{2}\text{erf}^{-1}\left(\frac{2\tilde{\gamma}_{\mathrm{u_f}}^{\varkappa_{\mathrm{u_f}}}}{\Gamma\left(\varkappa_{\mathrm{u_f}}\right)\varkappa_{\mathrm{u_f}}\varpi_{\mathrm{u_f}}^{\varkappa_{\mathrm{u_f}}}} - 1\right), \ldots, \sqrt{2}\text{erf}^{-1}\left(\frac{2\tilde{\gamma}_{\mathrm{u_f}}^{\varkappa_{\mathrm{u_f}}}}{\Gamma\left(\varkappa_{\mathrm{u_f}}\right)\varkappa_{\mathrm{u_f}}\varpi_{\mathrm{u_f}}^{\varkappa_{\mathrm{u_f}}}} - 1\right); \eta_{\mathrm{u_f}}\right) \tag{33}$$

in which (a) is achieved by inserting (7) and (8) into (21), $\tilde{\gamma}_{\text{sic}} = \frac{\hat{\gamma}_{\text{sic}}}{\overline{\gamma}\mu_{\text{c}}\left(p_{\mathrm{u_f}} - \hat{\gamma}_{\text{sic}}p_{\mathrm{u_n}}\right)}$, $\tilde{\gamma}_{\mathrm{u_n}} = \frac{\hat{\gamma}_{\mathrm{u_n}}}{\overline{\gamma}\mu_{\text{c}}p_{\mathrm{u_n}}}$, and $\tilde{\gamma}_{\max} = \max\left\{\tilde{\gamma}_{\text{sic}}, \tilde{\gamma}_{\mathrm{u_n}}\right\}$. Then, by utilizing the CDF of $g_{\text{fas},i}$ from (14), the proof is accomplished. □

Theorem 4. *The OP of the far FAS-equipped user* $\mathrm{u_f}$ *over the considered FAS-aided ISABC is given by* (26) *(see top of this page), in which*

$$\tilde{\gamma}_{\mathrm{u_f}} = \frac{\hat{\gamma}_{\mathrm{u_f}}}{\overline{\gamma}\mu_{\text{c}}\left(p_{\mathrm{u_f}} - \hat{\gamma}_{\mathrm{u_f}}p_{\mathrm{u_n}}\right)}. \tag{27}$$

Proof. By definition, the OP for the far user $\mathrm{u_2}$ is defined as

$$P_{\text{out},\mathrm{u_f}} = \Pr\left(\gamma_{\mathrm{u_f}} \leq \hat{\gamma}_{\mathrm{u_f}}\right), \tag{28}$$

where $\hat{\gamma}_{\mathrm{u_f}}$ is the SINR threshold of SINR $\gamma_{\mathrm{u_f}}$. Following the same approach as in the proof of Theorem 3, the OP for $\mathrm{u_f}$ when $p_{\mathrm{u_f}} > \hat{\gamma}_{\mathrm{u_f}}p_{\mathrm{u_n}}$ can be formulated as

$$P_{\text{out},\mathrm{u_f}} = \Pr\left(\frac{\overline{\gamma}p_{\mathrm{u_f}}\mu_{\text{c}}g_{\text{fas},\mathrm{u_f}}}{\overline{\gamma}p_{\mathrm{u_n}}\mu_{\text{c}}g_{\text{fas},\mathrm{u_f}} + 1} \leq \hat{\gamma}_{\mathrm{u_f}}\right) \tag{29}$$

$$= \Pr\left(g_{\text{fas},\mathrm{u_f}} \leq \frac{\hat{\gamma}_{\mathrm{u_f}}}{\overline{\gamma}\mu_{\text{c}}\left(p_{\mathrm{u_f}} - \hat{\gamma}_{\mathrm{u_f}}p_{\mathrm{u_n}}\right)}\right) \tag{30}$$

$$= F_{g_{\text{fas},\mathrm{u_f}}}\left(\frac{\hat{\gamma}_{\mathrm{u_f}}}{\overline{\gamma}\mu_{\text{c}}\left(p_{\mathrm{u_f}} - \hat{\gamma}_{\mathrm{u_f}}p_{\mathrm{u_n}}\right)}\right). \tag{31}$$

Now, by considering the CDF of $g_{\text{fas},i}$, (26) is obtained and the proof is completed. □

Corollary 1. *The asymptotic OP of the FAS-equipped users* $\mathrm{u_n}$ *and* $\mathrm{u_f}$ *in the high SNR regime, i.e.,* $\overline{\gamma} \to \infty$*, is given by* (32) *and* (33)*, respectively (see top of this page).*

Proof. By applying the relation of $\Upsilon\left(s, x\right) \approx x^s/s$ as $x \to 0$ to (14), the proof is accomplished. □

Remark 2. *The OP expressions in Theorems 3 and 4 are crucial for evaluating the likelihood of communication failure at both the near and far users in the proposed FAS-aided NOMA-ISABC system. OP is directly influenced by the allocation of power to each user and the presence of interference, and it provides an essential measure of system resilience under varying channel conditions. As will be confirmed later in Section V, the results will demonstrate that the proposed FAS setup yields significantly lower OP than the TAS configurations, suggesting that FAS enables dynamic reconfigurability to adapt to optimal positions, thereby mitigating interference more effectively. This adaptability makes FAS particularly advantageous for applications in mission-critical communication, such as real-time remote monitoring, where maintaining a low OP is essential for reliable data transmission. Moreover, the asymptotic analysis in Corollary 1 indicates that as the SNR increases, the OP approaches a lower bound, reinforcing the value of FAS in high-SNR scenarios often encountered in line-of-sight or high-power applications.*

2) ECR Analysis: The ECR of the proposed FAS-aided ISABC system with NOMA user i is defined as

$$\overline{\mathcal{C}}_i = \mathbb{E}\left[\log_2\left(1 + \gamma_i\right)\right] = \int_0^{\infty} \log_2\left(1 + \gamma_i\right) f_{\gamma_i}\left(\gamma_i\right) \mathrm{d}\gamma_i, \tag{34}$$

in which $f_{\gamma_i}\left(\gamma_i\right)$ is the PDF of γ_i that can be derived from (18). Therefore, by considering this, the ECR for NOMA user i is provided in the following theorem.

Theorem 5. *The ECR of FAS-equipped users* $\mathrm{u_n}$ *and* $\mathrm{u_f}$ *over the considered FAS-aided ISABC is, respectively, given by*

$$\overline{\mathcal{C}}_{\mathrm{u_n}} = \int_0^{\infty} \log_2\left(1 + \overline{\gamma}p_{\mathrm{u_n}}\mu_{\text{c}}g_{\text{fas},\mathrm{u_n}}\right) f_{g_{\text{fas},\mathrm{u_n}}}\left(g_{\text{fas},\mathrm{u_n}}\right) \mathrm{d}g_{\text{fas},\mathrm{u_n}}, \tag{35}$$

and

$$\overline{\mathcal{C}}_{\mathrm{u_f}} = \int_0^{\infty} \log_2\left(1 + \frac{\overline{\gamma}p_{\mathrm{u_f}}\mu_{\text{c}}g_{\text{fas},\mathrm{u_f}}}{\overline{\gamma}p_{\mathrm{u_n}}\mu_{\text{c}}g_{\text{fas},\mathrm{u_f}} + 1}\right) f_{g_{\text{fas},\mathrm{u_f}}}\left(g_{\text{fas},\mathrm{u_f}}\right) \mathrm{d}g_{\text{fas},\mathrm{u_f}}, \tag{36}$$

where $f_{g_{\text{fas},i}}\left(g_{\text{fas},i}\right)$ *is defined in* (18)*.*

Proof. Inserting (18) into (34) completes the proof. □

Computing the integrals in (35) and (36) is mathematically intractable since $f_{g_{\text{fas},i}}\left(g_{\text{fas},i}\right)$ is defined in terms of the PDF of multivariate and univariate normal distributions as given by

$$\overline{\mathcal{C}}_{\mathrm{u_n}} \approx \sum_{m=1}^{M} \sum_{n_{\mathrm{u_n}}=1}^{N_{\mathrm{u_n}}} w_m \mathrm{e}^{\epsilon_m} \log_2\left(1+\overline{\gamma} p_{\mathrm{u_n}} \mu_{\mathrm{c}} \epsilon_m\right) \frac{\partial \Phi_{\mathbf{R}_{\mathrm{u_n}}}\left(\tilde{\boldsymbol{\varphi}}^{-1}_{g^{N_{\mathrm{u_n}}}_{\mathrm{eq,u_n}}}\right)}{\partial \varphi^{-1}\left(F_{g^{n_{\mathrm{u_n}}}_{\mathrm{eq,u_n}}}(g_{\mathrm{fas}})\right)} \frac{f_{g^{n_{\mathrm{u_n}}}_{\mathrm{eq,u_n}}}(g_{\mathrm{fas}})}{\psi\left(\varphi^{-1}\left(F_{g^{n_{\mathrm{u_n}}}_{\mathrm{eq,u_n}}}(g_{\mathrm{fas}})\right)\right)} \tag{38}$$

$$\overline{\mathcal{C}}_{\mathrm{u_f}} \approx \sum_{m=1}^{M} \sum_{n_{\mathrm{u_f}}=1}^{N_{\mathrm{u_f}}} w_m \mathrm{e}^{\epsilon_m} \log_2\left(1+\frac{\overline{\gamma} p_{\mathrm{u_f}} \mu_{\mathrm{c}} \epsilon_m}{\overline{\gamma} p_{\mathrm{u_n}} \mu_{\mathrm{c}} \epsilon_m+1}\right) \frac{\partial \Phi_{\mathbf{R}_{\mathrm{u_f}}}\left(\breve{\boldsymbol{\varphi}}^{-1}_{g^{N_{\mathrm{u_f}}}_{\mathrm{eq,u_f}}}\right)}{\partial \varphi^{-1}\left(F_{g^{n_{\mathrm{u_f}}}_{\mathrm{eq,u_f}}}(g_{\mathrm{fas}})\right)} \frac{f_{g^{n_{\mathrm{u_f}}}_{\mathrm{eq,u_f}}}(g_{\mathrm{fas}})}{\psi\left(\varphi^{-1}\left(F_{g^{n_{\mathrm{u_f}}}_{\mathrm{eq,u_f}}}(g_{\mathrm{fas}})\right)\right)} \tag{39}$$

(18), which is quite complicated. Thus, the ECR needs to be solved numerically using multi-paradigm languages such as MATLAB. Additionally, it can be approximated mathematically by exploiting the numerical integration approaches such as the GLQ technique as defined in the following lemma.

Lemma 1. *The GLR for a function $\Lambda(x)$ in the real line domain $\mathbb{R}$, for some M, is defined as [58]*

$$\int_0^{\infty} \Lambda(x) dx \approx \sum_{m=1}^{M} w_m \mathrm{e}^{\epsilon_m} \Lambda(\epsilon_m), \tag{37}$$

where ϵ_m is the m-th root of Laguerre polynomial $L_M(\epsilon_m)$ and $w_m = \frac{\epsilon_m}{2(M+1)^2 L^2_{M+1}(\epsilon_m)}$ is the corresponding weight.

The GLQ method offers high accuracy for approximating integrals like $\int_0^{\infty} \Lambda(x) dx$, but it requires $\mathcal{O}(M^2)$ operations for an M-point quadrature, which can be computationally expensive in real-time wireless communication systems with limited resources. To address this issue, we consider the trade-off between accuracy and computational cost. By selecting a moderate value for M [59], we ensure that the computational cost remains manageable while the accuracy of the results is still within an acceptable range. This approach provides a practical solution that balances both efficiency and performance. For systems with more stringent resource constraints, further simplifications in the model could be considered to reduce computational overhead. However, in our current approach, the selected moderate range for M offers a sufficient balance between computational efficiency and the required accuracy, making the method feasible for real-time wireless communication systems with power or time limitations.

Corollary 2. *The ECR of the near FAS-equipped user u_{n} over the considered FAS-aided ISABC is given by (38) (see top of this page), in which*

$$\tilde{\boldsymbol{\varphi}}^{-1}_{g^{N_{\mathrm{u_n}}}_{\mathrm{eq,u_n}}} = \left[\sqrt{2}\mathrm{erf}^{-1}\left(\frac{2}{\Gamma(\varkappa_{\mathrm{u_n}})}\Upsilon\left(\varkappa_{\mathrm{u_n}}, \frac{\epsilon_m}{\varpi_{\mathrm{u_n}}}\right)-1\right), \ldots, \sqrt{2}\mathrm{erf}^{-1}\left(\frac{2}{\Gamma(\varkappa_{\mathrm{u_n}})}\Upsilon\left(\varkappa_{\mathrm{u_n}}, \frac{\epsilon_m}{\varpi_{\mathrm{u_n}}}\right)-1\right)\right].$$

Proof. By applying Lemma 1 to (35) and performing some simplifications, the proof is completed. □

Corollary 3. *The ECR of the far FAS-equipped user u_{f} over the considered FAS-aided ISABC is given by (39) (see top of this page), in which*

$$\breve{\boldsymbol{\varphi}}^{-1}_{g^{N_{\mathrm{u_f}}}_{\mathrm{eq,u_f}}} = \left[\sqrt{2}\mathrm{erf}^{-1}\left(\frac{2}{\Gamma(\varkappa_{\mathrm{u_f}})}\Upsilon\left(\varkappa_{\mathrm{u_f}}, \frac{\epsilon_m}{\varpi_{\mathrm{u_f}}}\right)-1\right), \ldots, 2\mathrm{erf}^{-1}\left(\frac{2}{\Gamma(\varkappa_{\mathrm{u_f}})}\Upsilon\left(\varkappa_{\mathrm{u_f}}, \frac{\epsilon_m}{\varpi_{\mathrm{u_f}}}\right)-1\right)\right].$$

Proof. By applying Lemma 1 to (36) and performing some simplifications, the proof is completed. □

Remark 3. *The ECR expressions for both near and far users in Corollaries 2 and 3 provide insight into the long-term average data rate achievable by the FAS-aided ISABC system. ECR is an important metric as it reflects the system's ability to sustain consistent data throughput, which is critical for applications that require continuous, high-data-rate transmission. As will be confirmed later in Section V, our analysis shows that the FAS-ISABC configurations yield higher ECR compared to conventional ISAC, due to the additional transmission path introduced by the backscatter tag. In practical terms, this improvement in ECR suggests that FAS-ISABC can better support high-throughput applications, in which maintaining a stable and high data rate is crucial for user experience.*

C. Sensing Performance

To evaluate sensing performance, we exploit the concept of estimation SR as defined in [54], where it is referred to as the radar estimation rate. While the terminology differs, both terms refer to the information rate at which the system can estimate the target's parameters, such as time-delay, which is a key indicator of target detection performance. In this sense, estimation SR in our work is conceptually equivalent to the radar estimation rate from [54], with the primary difference being the term used to describe the information-theoretic rate of target parameter estimation. From an information-theoretic viewpoint, estimation SR is analogous to the data information rate in wireless communication systems and represents the rate at which the system estimates target parameters. A higher SR indicates better performance in target detection. Therefore, given that the BS utilizes the received signal (3) to sense the TSR, the SR can be defined as

$$R_{\mathrm{t}} \leq \frac{\beta}{2T} \log_2\left(1+2T\gamma_{\mathrm{echo}}\right), \tag{40}$$

in which T denotes the radar pulse duration, β defines the radar's duty cycle, and γ_{echo} is the echo SNR, defined as

$$\gamma_{\mathrm{echo}} = \overline{\gamma}\zeta d_{\mathrm{t,b}}^{-\alpha} \left|h_{\mathrm{tsr,t}}\right|^2 \sigma^2_{\mathrm{echo}} = \frac{\pi^2}{3}\overline{\gamma}\zeta d_{\mathrm{t,b}}^{-\alpha} g_{\mathrm{t,b}} g_{\mathrm{b,t}} \sigma^2_{t_{\mathrm{df}}}, \tag{41}$$

where $g_{\mathrm{t,b}} = |h_{\mathrm{t,b}}|^2$ and $g_{\mathrm{b,t}} = |h_{\mathrm{b,t}}|^2$ are the channel gains from the tag to the BS and from the BS to the tag, respectively. Then we define the ESR to quantify the average estimation rate. This metric can be considered as the dual counterpart to the data information rate, denoted as

$$\begin{aligned}\overline{R}_{\mathrm{t}} &\leq \mathbb{E}\left[R_{\mathrm{t}}\right] \\ &= \frac{\beta}{2T}\int_0^{\infty} \log_2\left(1+2T\gamma_{\mathrm{echo}}\right) f_{\gamma_{\mathrm{echo}}}\left(\gamma_{\mathrm{echo}}\right) \mathrm{d}\gamma_{\mathrm{echo}}. \quad (42)\end{aligned}$$

Note that the SR metric is characterized by the CRLB for estimation, defined as $\sigma^2_{\mathrm{est}} \leq \frac{\sigma^2_{t_{\mathrm{df}}}}{2T\gamma_{\mathrm{echo}}}$, where σ^2_{est} is the time-delay estimation. In this regard, the ESR is first defined as

$$R_{\mathrm{t}} \leq \frac{H_{y_{\mathrm{b}}} - H_{\mathrm{est}}}{T_{\mathrm{bit}}}, \quad (43)$$

where $T_{\mathrm{bit}} = \frac{T}{\beta}$ represents the bits per pulse repetition interval, $H_{y_{\mathrm{b}}}$ and H_{est} denote the entropy of received signal and the entropy of errors, defined as $H_{y_{\mathrm{b}}} = \frac{1}{2}\log_2\left(2\pi \mathrm{e}\left(\sigma^2_{t_{\mathrm{df}}} + \sigma^2_{\mathrm{est}}\right)\right)$ and $H_{\mathrm{est}} = \frac{1}{2}\left(2\pi \mathrm{e}\sigma^2_{\mathrm{est}}\right)$, respectively. Therefore, the ESR is greatly affected by the radar's time-delay estimation, and it can be derived by exploiting the CRLB.

Theorem 6. *The ESR of the considered FAS-aided ISABC is given by*

$$\overline{R}_{\mathrm{t}} \leq \frac{\beta}{2T}\log_2\left(1+\frac{2}{3}T\bar{b}\bar{e}\pi^2\zeta d_{\mathrm{t,b}}^{-\alpha}\overline{\gamma}\sigma^2_{t_{\mathrm{df}}}\right), \quad (44)$$

where $\bar{e} = \mathbb{E}\left[g_{\mathrm{t,b}}\right]$.

Proof. See Appendix C. □

Remark 4. *ESR quantifies the system's capability to accurately detect and track environmental changes by estimating the time delay of backscattered signals, and is an appropriate metric for the proposed FAS-aided ISABC system, where simultaneous radar S&C are required. The derived ESR formula in (6) reveals that ESR is maximized when the power allocation for sensing is higher, but it decreases as the tag moves further from the BS due to increased path loss. This insight highlights the trade-off in power allocation between the S&C functions, which is a critical design consideration in ISABC systems.*

IV. Numerical Results

In this section, our derived analytical results are evaluated, which are double-checked in all instances by Monte Carlo simulations. To this end, we set the parameters as $p_{\mathrm{u_n}} = 0.3$, $p_{\mathrm{u_f}} = 0.7$, $\mu_{\mathrm{c}} = \mu_{\mathrm{s}} = 0.5$, $\zeta = 0.8$, $\overline{a} = \overline{b} = \overline{c} = \overline{e} = 1$, $\hat{\gamma}_{\mathrm{u_f}} = \hat{\gamma}_{\mathrm{u_n}} = \hat{\gamma}_{\mathrm{u_{sic}}} = 0$ dB, $d_{\mathrm{b,t}} = d_{\mathrm{b,u_n}} = 1$ m, $d_{\mathrm{b,u_f}} = 1.3$ m, $\alpha = 2.1$, $\beta = 0.5$, $\sigma^2_{t_{\mathrm{df}}} = 0.1$, and $T = 0.01$s. The chosen parameter values are both realistic and relevant to real-world applications, based on typical conditions found in the literature, with each parameter defined within its specific range. Furthermore, we utilize Algorithm 1 in [57] to simulate the Gaussian copula and its corresponding density functions.

We considered the following benchmarks for comparison:

- FAS-ISAC: ISAC with FAS-equipped users. This can be theoretically achieved by setting $\zeta = 0$ in (1) for communication performance without a backscatter tag

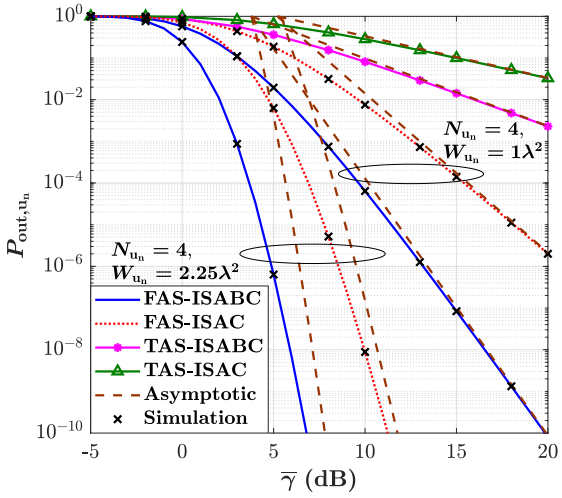

Fig. 4. OP versus average SNR $\overline{\gamma}$ for the near user $\mathrm{u_n}$, based on (19).

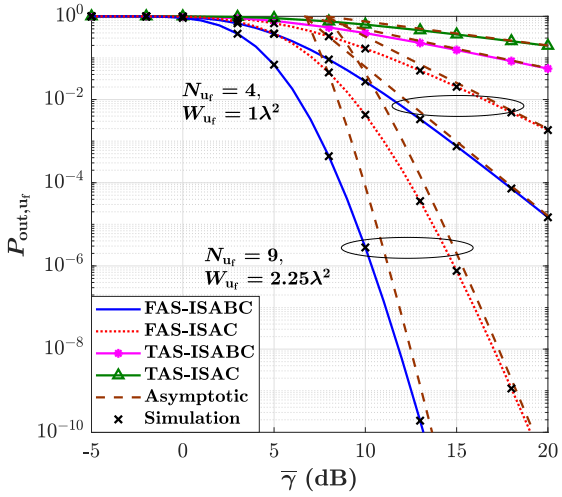

Fig. 5. OP versus average SNR $\overline{\gamma}$ for the far user $\mathrm{u_f}$, based on (26).

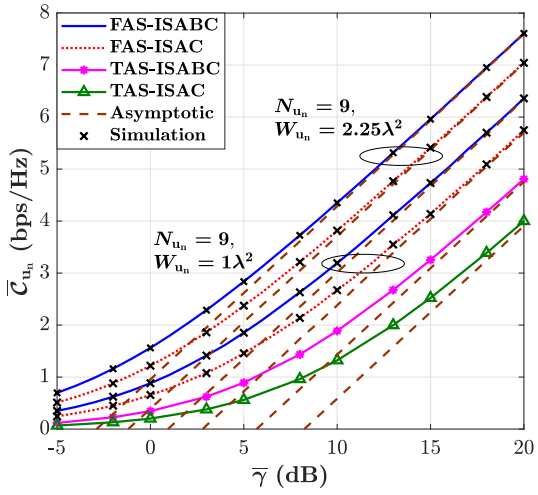

Fig. 6. ECR versus average SNR $\overline{\gamma}$ for the near user $\mathrm{u_n}$, based on (38).

This article has been accepted for publication in IEEE Internet of Things Journal. This is the author's version which has not been fully edited and content may change prior to final publication. Citation information: DOI 10.1109/JIOT.2025.3612478

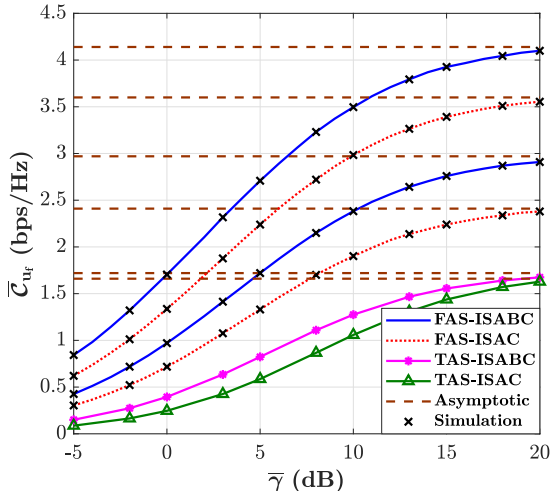

Fig. 7. ECR versus average SNR $\overline{\gamma}$ for the far user $\mathrm{u_f}$, based on (39).

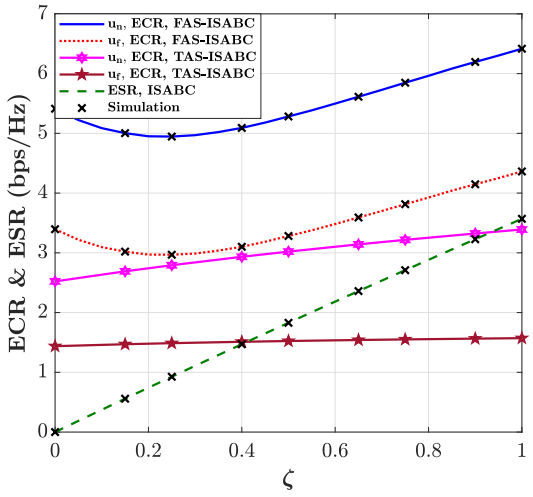

Fig. 9. Ergodic rate for both S&C versus tag's reflection coefficient ζ.

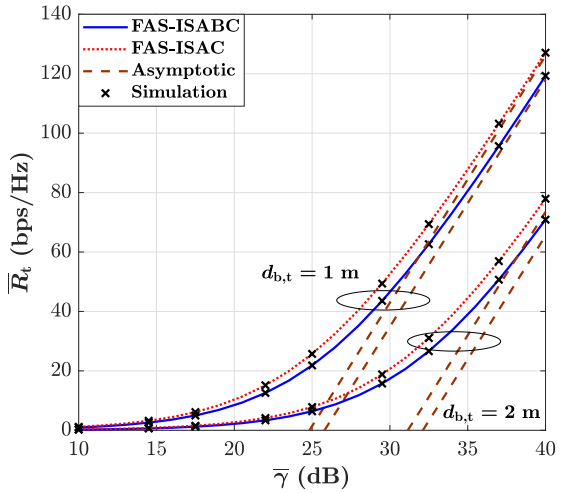

Fig. 8. ESR versus average SNR $\overline{\gamma}$ for different values of $d_{\mathrm{b,t}}$, based on (44).

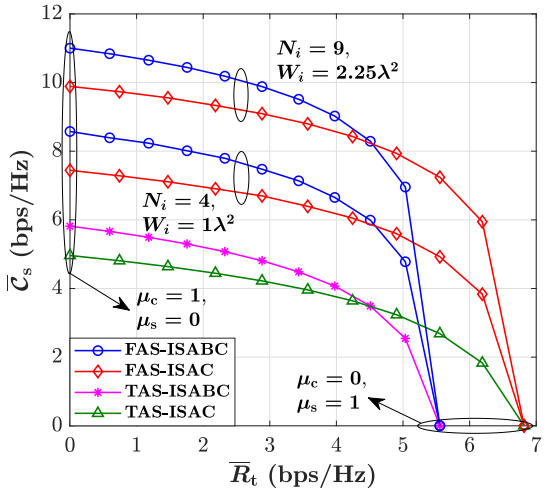

Fig. 10. ECR versus ESR for different μ and a given value of $\overline{\gamma} = 15$ dB.

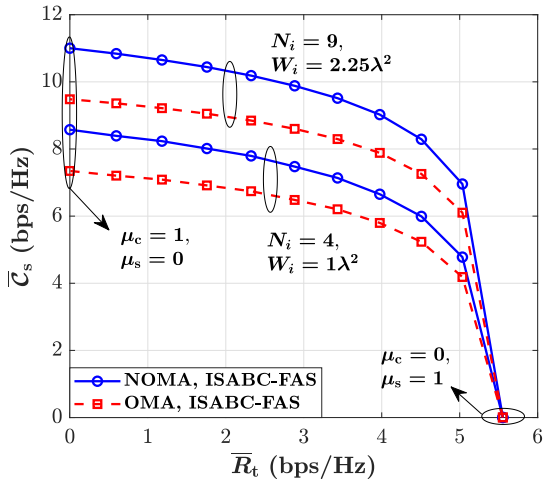

Fig. 11. ECR versus ESR comparison between NOMA and OMA.

and by setting $\zeta = 1$ in (3) for sensing performance with no reflection loss at the tag.

- TAS-ISABC: ISABC with TAS-equipped users.
- TAS-ISAC: ISAC with TAS-equipped users.

The OP performance againts the average SNR $\overline{\gamma}$ for near and far FAS-equipped users u_{n} and u_{f} are illustrated in Figs. 4 and 5, respectively, where the asymptotic results closely match the numerical results at high SNRs. First of all, in both figures, it can be observed that the proposed ISABC model provides a lower OP when the NOMA users are equipped with FAS rather than TAS. This is mainly due to the dynamic reconfigurability feature of FAS, allowing for real-time optimization of the antenna's performance based on the current environment and requirements. In this regard, we can also see that increasing the number of FAS ports N_i and the FAS size W_i significantly improves the OP performance for both NOMA users. Moreover, it is observed that the FAS-ISABC model improves the OP performance compared to ISAC with FAS-equipped users. This indicates that considering the backscatter tag is significantly more beneficial for communication performance

This article has been accepted for publication in IEEE Internet of Things Journal. This is the author's version which has not been fully edited and content may change prior to final publication. Citation information: DOI 10.1109/JIOT.2025.3612478

than for a conventional target. For instance, for FAS-equipped NOMA users $\mathrm{u_n}$ and $\mathrm{u_f}$ with $N_i = 4$ and $W_i = 1\lambda^2$ at $\overline{\gamma} = 10$dB, the OP under conventional ISAC is on the order of 10^{-2} and 10^{-1}, respectively, while the OP for ISABC-FAS is on the order of 10^{-4} and 10^{-2}. Furthermore, the asymptotic results indicate the accuracy of our theoretical analysis in the high SNR regime for both users.

In Figs. 6 and 7, the ECR performance versus $\overline{\gamma}$ is depicted for the near and far users $\mathrm{u_n}$ and $\mathrm{u_f}$, respectively. In both figures, the results show that the FAS-ISABC achieves higher ECR values compared to FAS-ISAC. This improvement is expected since the backscatter tag transmits additional data to the NOMA users, which can provide a higher CR for NOMA users. By carefully comparing the curves, we find that for the FAS-equipped users $\mathrm{u_n}$ and $\mathrm{u_f}$ having $N_i = 4$ and $W_i = 1\lambda^2$ at $\overline{\gamma} = 10$ dB, the ECR under ISABC is almost 15% and 20% higher than the ECR under FAS-ISAC for users $\mathrm{u_n}$ and $\mathrm{u_f}$, respectively. Furthermore, the results indicate that the FAS has significant effects on both the ISABC and conventional ISAC scenarios. For instance, under the same FAS configuration setup, the ECR provided by the FAS-ISABC for users $\mathrm{u_n}$ and $\mathrm{u_f}$ is almost 41% and 47% higher than that of TAS-ISABC for $\mathrm{u_n}$ and $\mathrm{u_f}$, respectively. Additionally, we see that the FAS-ISAC provides 50% and 45% higher ECR compared to TAS-ISAC for users $\mathrm{u_n}$ and $\mathrm{u_f}$, respectively. Furthermore, it is worth mentioning that such improvement can be enhanced when higher values of N_i and W_i are considered for the FAS setup or higher ζ is assumed for the backscatter tag over the communication stage. Moreover, at high SNR, we exploit the approximation of $\log_2(1+\mathrm{SNR}) \approx \log_2(\mathrm{SNR})$ in (38) and (39) to plot the asymptotic behaviour of the ECR. We see that the asymptotic curves reach the ECR at high SNR.

The ESR performance in terms of $\overline{\gamma}$ is illustrated in Fig. 8. It can be observed that the ISAC outperforms ISABC, as there is no reflection loss at the target, i.e., $\zeta = 1$. Additionally, as expected, the ESR decreases as the backscatter target is located farther away from the BS due to more severe path loss effects. Moreover, by using $\log_2(1+\mathrm{SNR}) \approx \log_2(\mathrm{SNR})$ for the high SNR regime in (44), the asymptotic results are provided that shows a perfect match with the ESR.

Fig. 9 illustrates the impact of the tag's reflection coefficient ζ on both the ECR and ESR. As mentioned, ζ controls the strength of the backscattered signal path in relation to the direct path from the BS to the NOMA users. It can be seen that for the FAS-ISABC, as ζ increases from 0, the backscatter path initially adds minimal or even disruptive interference, which can decrease the effective SNR for both users. Beyond a certain ζ threshold, however, the backscatter path strengthens enough to constructively combine with the direct path, boosting the received signal power and as a consequence, the ergodic capacity. More precisely, as ζ initially increases, the FAS may encounter intermediate reflection strengths, i.e., values of ζ, that are not yet optimal, leading to non-monotonic capacity behavior, namely the ECR may decrease temporarily as the system adjusts to the evolving signal environment. To clarify, this behavior is not due to the tag's physical position, but rather to intermediate values of the reflection coefficient ζ, where the backscatter path is too weak to combine constructively with the direct path and may instead introduce disruptive interference. As ζ increases further, the FAS is better able to align with both signal components, improving the overall ECR. Once ζ reaches a point where the backscatter path provides constructive interference, the FAS can leverage its adaptability to align with both paths effectively, leading to an increase in capacity. By contrast, in the TAS-ISABC, the users have no spatial flexibility or adaptive capability to optimize signal reception. Hence, as ζ increases, the single antenna passively accumulates more signal power from the strengthening backscatter path, leading to a monotonic increase in ECR. This behavior is straightforward because the TAS simply benefits from the additional power without the ability to mitigate any intermediate interference effects. Additionally, we can see that the ESR continuously increases as ζ grows. The reason behind this trend is that as ζ increases, the reflection loss at the tag decreases, allowing the backscatter path to progressively approach full enablement, thereby enhancing the signal strength available for sensing.

Fig. 10 characterizes the performance interplay between the ECR and the ESR for a given average SNR $\overline{\gamma}$. Specifically, by allocating different power coefficients μ_χ at the BS for communication and sensing stages, we plot the sum of ECR (i.e., $\overline{\mathcal{C}}_\mathrm{s} = \overline{\mathcal{C}}_{\mathrm{u_n}} + \overline{\mathcal{C}}_{\mathrm{u_f}}$) for both NOMA users in terms of the ESR. To do so, we set $\mu_\mathrm{c} = \mu$, and therefore $\mu_\mathrm{s} = 1-\mu$, and change the power coefficient μ from 0 to 1. In this regard, by carefully comparing the curves, it can be observed that both ergodic rates (i.e, communication and sensing) achieved by TAS-ISABC and TAS-ISAC are always lower than those achievable by FAS-ISABC and FAS-ISAC, respectively, which confirms the superiority of FAS compared to TAS.

Furthermore, FAS-ISABC and TAS-ISABC perform better (worse) in terms of the communication (sensing) rate compared with conventional FAS-ISAC and TAS-ISAC, respectively. Therefore, for both the ISABC and ISAC scenarios, this specific behaviour highly depends on the value of power coefficient at the BS, where larger (smaller) μ causes higher (lower) CR and lower (higher) SR. More precisely, the ESR is zero when $\mu = 1$ since all the power is utilized for communication stage and no power is considered for target detection. Thus, we reach non-zero ECR with zero ESR. Additionally, by assuming $\mu = 0$, the highest value of ESR is achieved, while the ECR cannot be reduced to zero due to the ISAC principle. Hence, it is concluded that without any CR constraints, the SR is maximized with the available transmit power. Conversely, when NOMA users require a non-zero CR, the power coefficient tends to diminish the SR.

To further validate the role of NOMA in FAS-assisted ISABC systems, we compare its performance with orthogonal multiple access (OMA) in Fig. 11, under identical system assumptions. As seen, NOMA consistently provides higher sensing and communication rates compared to OMA for all resource-splitting configurations, i.e., μ_c and μ_s. The gain is more significant when communication is prioritized, owing to the superior spectrum utilization and power-domain multiplexing of NOMA. This comparison confirms the advantage of integrating NOMA with FAS-ISABC, aligning with prior results in the literature.

V. Conclusion

In this paper, we studied the performance of a FAS-aided ISABC system under NOMA. Specifically, we consider an ISABC scenario in which a backscatter tag provides sensing information to the BS while simultaneously transmitting additional data to the FAS-equipped NOMA users. For the proposed model, we first derive closed-form expressions for the CDF and PDF of the equivalent channel at both NOMA users using moment matching techniques and the Gaussian copula. Then, we obtain closed-form expressions for the OP and the corresponding asymptotic derivations in the high SNR regime. Additionally, we approximate the ECR using the numerical integration GLQ technique. Moreover, we derive the ESR in closed form via the CRLB. Eventually, our numerical results provide useful insights into achieving an accurate trade-off between SR and CR. Furthermore, they demonstrate that FAS significantly enhances the overall performance of both conventional ISAC and ISABC compared to TAS. Building on these findings, future work could investigate high-mobility scenarios, multiuser or multi-tag configurations, and physical layer security. These extensions would aim to further enhance the robustness, scalability, and security of ISABC systems, particularly in dynamic and complex environments. An interesting direction for future work is to investigate the integration of RSMA into the FAS-aided ISABC framework. RSMA's enhanced robustness to channel uncertainty and potential for user fairness could offer further performance gains, particularly in centralized or coordinated ISAC scenarios. Besides, future research may explore the integration of FAS with other emerging physical layer technologies such as massive MIMO and RIS, potentially enabling hybrid ISAC architectures that combine infrastructure-side intelligence with user-end adaptability.

Appendix A
Proof of Theorem 1

Given (1), the equivalent channel at the n_i-th port of user i is given by $g_{\mathrm{eq},i}^{n_i} = d_{\mathrm{b},i}^{-\alpha} g_{\mathrm{b},i}^{n_i} + \zeta d_{\mathrm{b,t}}^{-\alpha} d_{\mathrm{t},i}^{-\alpha} g_{\mathrm{b,t}} g_{\mathrm{t},i}^{n_i}$. Without loss of generality and for ease of display, we consider

$$g_{\mathrm{eq},i}^{n_i} = d_{\mathrm{b},i}^{-\alpha} A + \zeta d_{\mathrm{b,t}}^{-\alpha} d_{\mathrm{t},i}^{-\alpha} BC = A' + D, \tag{45}$$

where, given that all channels undergo Rayleigh fading, the channel gains follow exponential distributions. Hence, we have the PDF and CDF for the channel gain $R \in \{A, B, C\}$ as [55]

$$\begin{cases} f_R(r) = \dfrac{1}{\overline{r}} \exp\left(-\dfrac{r}{\overline{r}}\right), \\ F_R(r) = 1 - \exp\left(-\dfrac{r}{\overline{r}}\right), \end{cases} \tag{46}$$

in which $\overline{r} = \mathbb{E}[R]$ is the expected value of the RV R for $r \in \{a, b, c\}$. To derive the distribution of $g_{\mathrm{eq},i}^{n_i}$, we first obtain the distribution RV $D = \zeta d_{\mathrm{b,t}}^{-\alpha} d_{\mathrm{t},i}^{-\alpha} BC$, which involves the product of two exponentially-distributed RVs. Hence, by using the definition, we have

$$F_D(d) = \int_0^\infty f_B(b) F_C\left(\frac{d_{\mathrm{b,t}}^{\alpha} d_{\mathrm{t},i}^{\alpha} d}{\zeta b}\right) \mathrm{d}b \tag{47}$$

$$\overset{(a')}{=} 1 - \frac{1}{\overline{b}} \int_0^\infty \exp\left(-\left(\frac{b}{\overline{b}} + \frac{d_{\mathrm{b,t}}^{\alpha} d_{\mathrm{t},i}^{\alpha} d}{\zeta b \overline{c}}\right)\right) \mathrm{d}b \tag{48}$$

$$\overset{(b')}{=} 1 - 2\sqrt{\frac{d_{\mathrm{b,t}}^{\alpha} d_{\mathrm{t},i}^{\alpha} d}{\zeta \overline{b}\overline{c}}} \mathcal{K}_1\left(2\sqrt{\frac{d_{\mathrm{b,t}}^{\alpha} d_{\mathrm{t},i}^{\alpha} d}{\zeta \overline{b}\overline{c}}}\right), \tag{49}$$

where (a') is obtained by considering the univariate marginal distributions from (46) and (b') is derived by utilizing the integral format provided in [60, 3.471.9]. In (49), $\mathcal{K}_\nu(\cdot)$ represents the ν-order modified Bessel function of the second kind. Then, by utilizing the PDF definition $f(d) = \frac{\partial}{\partial d} F_D(d)$, the corresponding PDF can be formulated as

$$f_D(d) = \frac{2 d_{\mathrm{b,t}}^{\alpha} d_{\mathrm{t},i}^{\alpha}}{\zeta \overline{b}\overline{c}} \mathcal{K}_0\left(2\sqrt{\frac{d_{\mathrm{b,t}}^{\alpha} d_{\mathrm{t},i}^{\alpha} d}{\zeta \overline{b}\overline{c}}}\right). \tag{50}$$

Next, the distribution of $g_{\mathrm{eq},i}^{n_i} = A' + D$, which includes the sum of two independent RVs, can be defined as

$$F_{g_{\mathrm{eq},i}^{n_i}}(g_{\mathrm{eq}}) = \int_0^\infty F_{A'}(g_{\mathrm{eq}} - d) f_D(d) \, \mathrm{d}d. \tag{51}$$

However, deriving an exact statistical characterization of the CDF in (51) seems challenging. To overcome this issue, we resort to the moment matching technique to approximate the corresponding CDF [61]. In this context, the gamma distribution is often utilized to approximate complex distributions due to its simplicity, characterized only by two adjustable parameters: the shape parameter $\varkappa$ and the scale parameter ϖ. Thus, the mean and variance of such approximation gamma distribution are defined as $\varkappa\varpi$ and $\varkappa\varpi^2$, respectively.

Now, let us attempt to find the CDF of $g_{\mathrm{eq},i}^{n_i}$ using the moment matching technique. By definition, the mean and variance of D can be calculated as $\mathbb{E}[D] = \zeta d_{\mathrm{b,t}}^{-\alpha} d_{\mathrm{t},i}^{-\alpha} \overline{b}\overline{c}$ and $\mathrm{Var}(D) = 3\left(\zeta d_{\mathrm{b,t}}^{-\alpha} d_{\mathrm{t},i}^{-\alpha} \overline{b}\overline{c}\right)^2$, respectively. Similarly, the mean and variance of A' are given by $\mathbb{E}[A'] = d_{\mathrm{b},i}^{-\alpha} \overline{a}$ and $\mathrm{Var}(A') = d_{\mathrm{b},i}^{-2\alpha} \overline{a}^2$, respectively. Now, by matching the mean and variance of the RV $g_{\mathrm{eq},i}^{n_i} = A' + D$ with the mean $\varkappa_i \varpi_i$ and variance $\varkappa_i \varpi_i^2$ of the gamma distribution, we have

$$F_{g_{\mathrm{eq},i}^{n_i}}(g_{\mathrm{eq}}) \approx \frac{1}{\Gamma(\varkappa_i)} \Upsilon\left(\varkappa_i, \frac{g_{\mathrm{eq}}}{\varpi_i}\right), \tag{52}$$

in which

$$\varkappa_i = \frac{d_{\mathrm{b},i}^{-2\alpha} \overline{a}^2 + 3\left(\zeta d_{\mathrm{b,t}}^{-\alpha} d_{\mathrm{t},i}^{-\alpha} \overline{b}\overline{c}\right)^2}{d_{\mathrm{b},i}^{-\alpha} \overline{a} + \zeta d_{\mathrm{b,t}}^{-\alpha} d_{\mathrm{t},i}^{-\alpha} \overline{b}\overline{c}} \tag{53}$$

and

$$\varpi_i = \frac{\left(d_{\mathrm{b},i}^{-\alpha} \overline{a} + \zeta d_{\mathrm{b,t}}^{-\alpha} d_{\mathrm{t},i}^{-\alpha} \overline{b}\overline{c}\right)^2}{d_{\mathrm{b},i}^{-2\alpha} \overline{a}^2 + 3\left(\zeta d_{\mathrm{b,t}}^{-\alpha} d_{\mathrm{t},i}^{-\alpha} \overline{b}\overline{c}\right)^2}. \tag{54}$$

Furthermore, by extending the joint CDF definition, the CDF of $g_{\mathrm{fas},i}$ can be mathematically expressed as

$$\begin{aligned} &F_{\mathrm{fas},i}\left(g_{\mathrm{fas}}\right) \\ &= \Pr\left(\max\left\{g_{\mathrm{eq},i}^{1},\ldots,g_{\mathrm{eq},i}^{N_i}\right\} \le g_{\mathrm{fas}}\right) && (55)\\ &= \Pr\left(g_{\mathrm{eq},i}^{1} \le g_{\mathrm{fas}},\ldots,g_{\mathrm{eq},i}^{N_i} \le g_{\mathrm{fas}}\right) && (56)\\ &= F_{g_{\mathrm{eq},i}^{1},\ldots,g_{\mathrm{eq},i}^{N_i}}\left(g_{\mathrm{fas}},\ldots,g_{\mathrm{fas}}\right) && (57)\\ &\overset{(c')}{=} C\left(F_{g_{\mathrm{eq},i}^{1}}\left(g_{\mathrm{fas}}\right),\ldots,F_{g_{\mathrm{eq},i}^{N_i}}\left(g_{\mathrm{fas}}\right);\vartheta_i\right) && (58)\\ &\overset{(d')}{=} \mathbf{\Phi}_{\mathbf{R}_i}\left(\varphi^{-1}\left(F_{g_{\mathrm{eq},i}^{1}}\left(g_{\mathrm{fas}}\right)\right),\ldots,\varphi^{-1}\left(F_{g_{\mathrm{eq},i}^{N_i}}\left(g_{\mathrm{fas}}\right)\right);\eta_i\right), && (59)\end{aligned}$$

where (c') is obtained by using Sklar's theorem from (10), and (d') is determined by considering the definition of Gaussian copula, where $\varphi^{-1}(\cdot)$ is defined as

$$\varphi^{-1}\left(F_{g_{\mathrm{eq},i}^{n_i}}\left(g_{\mathrm{fas}}\right)\right) = \sqrt{2}\mathrm{erf}^{-1}\left(2F_{g_{\mathrm{eq},i}^{n_i}}\left(g_{\mathrm{fas}}\right)-1\right). \quad (60)$$

Eventually, by substituting (52) into (60), and then inserting the results into (59), we derive (14) and complete the proof.

Appendix B
Proof of Theorem 2

By applying the chain rule to (14), the PDF of g_{fas} is expressed as (18). Hence, we need to derive the PDF of $g_{\mathrm{eq},i}^{n_i}$. By applying the PDF definition $f_X(x) = \frac{\partial}{\partial X}F_X(x)$ to (52), we have

$$f_{g_{\mathrm{eq},i}^{n_i}}\left(g_{\mathrm{eq}}\right) = \frac{1}{\Gamma\left(\varkappa\right)\varpi^{\varkappa}} g_{\mathrm{eq}}^{\varkappa-1}\mathrm{e}^{-\frac{g_{\mathrm{eq}}}{\varpi}}. \quad (61)$$

Now, by substituting (13), (52), and (61) into (18), we get the desired result and the proof is accomplished.

Appendix C
Proof of Theorem 6

In order to derive $\overline{R}_{\mathrm{t}}$, we need to solve the integral in (42), which mathematically defines the ESR. To accomplish this, we apply Jensen's inequality so that (42) can be rewritten as

$$\overline{R} \le \frac{\beta}{2T}\log_2\left(1+2T\mathbb{E}\left[\gamma_{\mathrm{echo}}\right]\right), \quad (62)$$

where $\mathbb{E}\left[\gamma_{\mathrm{echo}}\right]$ is the expected value of γ_{echo}. Next, we need to find the PDF of γ_{echo}. In (41), since γ_{echo} involves the product of two exponentially-distributed channel gains $g_{\mathrm{b,t}}$ and $g_{\mathrm{t,b}}$, the PDF of γ_{echo} can be directly derived from (50), i.e.,

$$f_{\gamma_{\mathrm{echo}}}\left(\gamma_{\mathrm{echo}}\right) = \frac{6d_{\mathrm{t,b}}^{\alpha}}{\overline{b}\overline{e}\pi^2\overline{\gamma}\zeta\sigma_{t_{\mathrm{df}}}^2}\mathcal{K}_0\left(2\sqrt{\frac{3\gamma_{\mathrm{echo}}d_{\mathrm{t,b}}^{\alpha}}{\overline{b}\overline{e}\pi^2\overline{\gamma}\zeta\sigma_{t_{\mathrm{df}}}^2}}\right), \quad (63)$$

where $\overline{e} = \mathbb{E}\left[g_{\mathrm{t,b}}\right]$. Hence, $\mathbb{E}\left[\gamma_{\mathrm{echo}}\right]$ is given by

$$\begin{aligned} \mathbb{E}\left[\gamma_{\mathrm{echo}}\right] &= \int_0^{\infty}\frac{6\gamma_{\mathrm{echo}}d_{\mathrm{t,b}}^{\alpha}}{\overline{b}\overline{e}\pi^2\overline{\gamma}\zeta\sigma_{t_{\mathrm{df}}}^2}\mathcal{K}_0\left(2\sqrt{\frac{3\gamma_{\mathrm{echo}}d_{\mathrm{t,b}}^{\alpha}}{\overline{b}\overline{e}\pi^2\overline{\gamma}\zeta\sigma_{t_{\mathrm{df}}}^2}}\right)\mathrm{d}\gamma_{\mathrm{echo}} && (64)\\ &= \frac{1}{3}\overline{b}\overline{e}\pi^2\overline{\gamma}\zeta d_{\mathrm{t,b}}^{-\alpha}\sigma_{t_{\mathrm{df}}}^2. && (65)\end{aligned}$$

Now, by substituting (65) into (62), (44) is achieved.

References

[1] F. Tariq *et al.*, "A speculative study on 6G," *IEEE Wireless Commun.*, vol. 27, no. 4, pp. 118–125, Aug. 2020.

[2] X. You *et al.*, "Toward 6G TKμ extreme connectivity: Architecture, key technologies and experiments," *IEEE Wireless Commun.*, vol. 30, no. 3, pp. 86–95, Jun. 2023.

[3] F. Guo *et al.*, "Enabling Massive IoT Toward 6G: A Comprehensive Survey," *IEEE Internet Things J.*, vol. 8, no. 15, pp. 11891–11915, 1 Aug.1, 2021.

[4] F. Liu *et al.*, "Integrated sensing and communications: Toward dual-functional wireless networks for 6G and beyond," *IEEE J. Select. Areas Commun.*, vol. 40, no. 6, pp. 1728–1767, Jun. 2022.

[5] J. A. Zhang *et al.*, "An overview of signal processing techniques for joint communication and radar sensing," *IEEE J. Select. Topics Sig. Proc.*, vol. 15, no. 6, pp. 1295–1315, Nov. 2021.

[6] J. A. Zhang *et al.*, "Enabling joint communication and radar sensing in mobile networks—A survey," *IEEE Commun. Surv. & Tut.*, vol. 24, no. 1, pp. 306–345, Firstquarter 2022.

[7] Y. Cui, F. Liu, X. Jing and J. Mu, "Integrated Sensing and Communications (ISAC) for Vehicular Communication Networks (VCN),," *IEEE Internet Things J.*, vol. 9, no. 23, pp. 23441–23451, 1 Dec.1, 2022.

[8] K. K. Wong, A. Shojaeifard, K. F. Tong, and Y. Zhang, "Performance limits of fluid antenna systems," *IEEE Commun. Lett.*, vol. 24, no. 11, pp. 2469–2472, Nov. 2020.

[9] K. K. Wong, A. Shojaeifard, K. F. Tong, and Y. Zhang, "Fluid antenna systems," *IEEE Trans. Wireless Commun.*, vol. 20, no. 3, pp. 1950–1962, Mar. 2021.

[10] K. K. Wong, K. F. Tong, Y. Shen, Y. Chen, and Y. Zhang, "Bruce Lee-inspired fluid antenna system: Six research topics and the potentials for 6G," *Frontiers Commun. and Netw., section Wireless Commun.*, vol. 3, no. 853416, Mar. 2022.

[11] M. Khammassi, A. Kammoun and M.-S. Alouini, "A new analytical approximation of the fluid antenna system channel," *IEEE Trans. Wireless Commun.*, vol. 22, no. 12, pp. 8843–8858, Dec. 2023.

[12] J. D. Vega-Sánchez, A. E. López-Ramírez, L. Urquiza-Aguiar and D. P. M. Osorio, "Novel expressions for the outage probability and diversity gains in fluid antenna system," *IEEE Wireless Commun. Lett.*, vol. 13, no. 2, pp. 372–376, Feb. 2024.

[13] J. D. Vega-Sánchez, L. Urquiza-Aguiar, M. C. P. Paredes and D. P. M. Osorio, "A simple method for the performance analysis of fluid antenna systems under correlated Nakagami-m fading," *IEEE Wireless Commun. Lett.*, vol. 13, no. 2, pp. 377–381, Feb. 2024.

[14] P. D. Alvim *et al.*, "On the performance of fluid antennas systems under α-μ fading channels," *IEEE Wireless Commun. Lett.*, vol. 13, no. 1, pp. 108–112, Jan. 2024.

[15] C. Psomas, P. J. Smith, H. A. Suraweera and I. Krikidis, "Continuous fluid antenna systems: Modeling and analysis," *IEEE Commun. Lett.*, vol. 27, no. 12, pp. 3370–3374, Dec. 2023.

[16] W. K. New, K. K. Wong, H. Xu, K. F. Tong and C.-B. Chae, "An information-theoretic characterization of MIMO-FAS: Optimization, diversity-multiplexing tradeoff and q-outage capacity," *IEEE Trans. Wireless Commun.*, vol. 23, no. 6, pp. 5541–5556, Jun. 2024.

[17] H. Xu *et al.*, "Channel estimation for FAS-assisted multiuser mmWave systems," *IEEE Commun. Lett.*, vol. 28, no. 3, pp. 632–636, Mar. 2024.

[18] Z. Zhang, J. Zhu, L. Dai, and R. W. Heath Jr, "Successive Bayesian reconstructor for channel estimation in fluid antenna systems," *IEEE Trans. Wireless Commun.*, vol. 24, no. 3, pp. 1992-2006, March 2025.

[19] J. Zou, S. Sun and C. Wang, "Online learning-induced port selection for fluid antenna in dynamic channel environment," *IEEE Wireless Commun. Lett.*, vol. 13, no. 2, pp. 313–317, Feb. 2024.

[20] C. Wang *et al.*, "AI-empowered fluid antenna systems: Opportunities, challenges, and future directions," *IEEE Wireless Commun.*, vol. 31, no. 5, pp. 34–41, Oct. 2024.

[21] N. Waqar *et al.*, "Opportunistic fluid antenna multiple access via team-inspired reinforcement learning," *IEEE Trans. Wireless Commun.*, vol. 23, no. 9, pp. 12068–12083, Sept. 2024.

[22] L. Zhu, and K. K. Wong, "Historical review of fluid antennas and movable antennas," *arXiv preprint*, arXiv:2401.02362v2, Jan. 2024.

[23] Y. Shen *et al.*, "Design and implementation of mmWave surface wave enabled fluid antennas and experimental results for fluid antenna multiple access," *arXiv preprint*, arXiv:2405.09663, May 2024.

[24] J. Zhang *et al.*, "A novel pixel-based reconfigurable antenna applied in fluid antenna systems with high switching speed," *IEEE Open J. Antennas & Propag.*, doi:10.1109/OJAP.2024.3489215, 2024.

[25] X. Lu *et al.*, "Ambient backscatter assisted wireless powered communications," *IEEE Wireless Commun.*, vol. 25, no. 2, pp. 170–177, Apr. 2018.

[26] G. Yang, Q. Zhang and Y. -C. Liang, "Cooperative Ambient Backscatter Communications for Green Internet-of-Things," *IEEE Internet Things J.*, vol. 5, no. 2, pp. 1116–1130, April 2018.

[27] I. F. Akyildiz, A. Kak, and S. Nie, "6G and beyond: The future of wireless communications systems," *IEEE Access*, vol. 8, pp. 133 995–134 030, Jul. 2020.

[28] F. Jameel *et al.*, "NOMA-Enabled Backscatter Communications: Toward Battery-Free IoT Networks," *IEEE Internet Things Mag.*, vol. 3, no. 4, pp. 95-101, Dec. 2020.

[29] M. Ahmed *et al.*, "NOMA-Based Backscatter Communications: Fundamentals, Applications, and Advancements," *IEEE Internet Things J.*, vol. 11, no. 11, pp. 19303-19327, June, 2024.

[30] M. Asif *et al.*, "Energy-Efficient Backscatter-Assisted Coded Cooperative NOMA for B5G Wireless Communications," *IEEE Trans. Green Commun. Netw.*, vol. 7, no. 1, pp. 70-83, March 2023.

[31] C. Ouyang, Y. Liu, and H. Yang, "Performance of downlink and uplink integrated sensing and communications (ISAC) systems," *IEEE Wireless Commun. Lett.*, vol. 11, no. 9, pp. 1850–1854, Sept. 2022.

[32] C. Ouyang, Y. Liu, and H. Yang, "On the performance of uplink ISAC systems," *IEEE Commun. Lett.*, vol. 26, no. 8, pp. 1769–1773, Aug. 2022.

[33] C. Ouyang, Y. Liu, and H. Yang, "MIMO-ISAC: Performance analysis and rate region characterization," *IEEE Wireless Commun. Lett.*, vol. 12, no. 4, pp. 669–673, Apr. 2023.

[34] M. Liu *et al.*, "Performance analysis and power allocation for cooperative ISAC networks," *IEEE Int. Things J.*, vol. 10, no. 7, pp. 6336–6351, Apr. 2023.

[35] Z. Wang, Y. Liu, X. Mu, Z. Ding, and O. A. Dobre, "NOMA empowered integrated sensing and communication," *IEEE Commun. Lett.*, vol. 26, no. 3, pp. 677–681, Mar. 2022.

[36] C. Ouyang, Y. Liu, and H. Yang, "Revealing the impact of SIC in NOMA-ISAC," *IEEE Wireless Commun. Lett.*, vol. 12, no. 10, pp. 1707–1711, Oct. 2023.

[37] C. Zhang, W. Yi, Y. Liu, and L. Hanzo, "Semi-integrated-sensing-and-communication (semi-ISaC): From OMA to NOMA," *IEEE Trans. Commun.*, vol. 71, no. 4, pp. 1878–1893, Apr. 2023.

[38] B. Zhao, C. Ouyang, Y. Liu, X. Zhang, and H. V. Poor, "Modeling and analysis of near-field ISAC," *IEEE J. Select. Topics Sig. Proc.*, early access, DOI:10.1109/JSTSP.2024.3386054, Apr. 2024.

[39] W. K. New *et al.*, "Fluid antenna system enhancing orthogonal and non-orthogonal multiple access," *IEEE Commun. Lett.*, vol. 28, no. 1, pp. 218–222, Jan. 2024.

[40] F. R. Ghadi *et al.*, "On performance of FAS-aided wireless powered NOMA communication systems," *2024 20th International Conference on Wireless and Mobile Computing, Networking and Communications (WiMob)*, Paris, France, 2024, pp. 496–501.

[41] Q. Zhang, M. Shao, T. Zhang, G. Chen, and J. Liu, "An efficient algorithm for sum-rate maximization in fluid antenna-assisted ISAC system," *arXiv preprint*, arXiv:2405.06516, May 2024.

[42] C. Wang *et al.*, "Fluid antenna system liberating multiuser MIMO for ISAC via deep reinforcement learning," *IEEE Trans. Wireless Commun.*, vol. 23, no. 9, pp. 10 879–10 894, Sep. 2024.

[43] F. R. Ghadi, M. Kaveh, K.-K. Wong, and Y. Zhang, "Performance analysis of FAS-aided backscatter communications," *IEEE Wireless Commun. Lett.*, vol. 13, no. 9, pp. 2412–2416, Sept. 2024.

[44] D. Galappaththige, C. Tellambura, and A. Maaref, "Integrated sensing and backscatter communication," *IEEE Wireless Commun. Lett.*, vol. 12, no. 12, pp. 2043–2047, Dec. 2023.

[45] Z. Zhao, Y. Dong, T. Wei, X. P. Zhang, X. Tang, and Z. Liu, "B-ISAC: Backscatter integrated sensing and communication for 6G IoE applications," *arXiv preprint*, arXiv:2407.19235v2, Nov. 2024.

[46] H. Luo, U. Demirhan, and A. Alkhateeb, "ISAC with backscattering RFID tags: Joint beamforming design," *ICC 2024 - IEEE International Conference on Communications*, Denver, CO, USA, 2024, pp. 921-925.

[47] S. Zargari, D. Galappaththige, and C. Tellambura, "Transmit Power-Efficient Beamforming Design for Integrated Sensing and Backscatter Communication," *IEEE Open Journal of the Communications Society*, vol. 6, pp. 775-792, 2025.

[48] L. Venturino, E. Grossi, M. Lops, J. Johnston and X. Wang, "Radar-enabled ambient backscatter communications," *IEEE Trans. Wireless Commun.*, vol. 22, no. 12, pp. 8666–8680, Dec. 2023.

[49] L. Venturino, E. Grossi, J. Johnston, M. Lops and X. Wang, "Joint data and channel estimation in radar-enabled backscatter communications," in *Proc. IEEE Int. Workshop Tech. Defense & Security (TechDefense)*, pp. 368–372, 20-22 Nov. 2023, Rome, Italy.

[50] R. K, R. Allu, K. Singh, C. -P. Li and S. Biswas, "Optimized Resource Allocation in NOMA-Enabled ISAC Systems With RFID Backscatterers," *IEEE Wireless Commun. Lett.*, vol. 14, no. 7, pp. 1934-1938, July 2025.

[51] D. Galappaththige, S. Zargari, C. Tellambura and G. Y. Li, "Optimization of Rate-Splitting Multiple Access With Integrated Sensing and Backscatter Communication," *IEEE IEEE Trans. Veh. Technol.*, vol. 74, no. 6, pp. 9117-9133, June 2025.

[52] K.-K. Wong, K.-F. Tong, Y. Chen, and Y. Zhang, "Fast fluid antenna multiple access enabling massive connectivity," *IEEE Commun. Lett.*, vol. 27, no. 2, pp. 711–715, 2022.

[53] K. K. Wong, C. B. Chae and K. F. Tong, "Compact ultra massive antenna array: A simple open-loop massive connectivity scheme," *IEEE Trans. Wireless Commun.*, vol. 23, no. 6, pp. 6279–6294, Jun. 2024.

[54] A. R. Chiriyath, B. Paul, G. M. Jacyna, and D. W. Bliss, "Inner bounds on performance of radar and communications co-existence," *IEEE Trans. Sig. Proc.*, vol. 64, no. 2, pp. 464–474, Jan. 2016.

[55] T. .S. Rappaport, *Wireless communications: principles and practice*, Cambridge University Press, 2024.

[56] F. R. Ghadi and G. A. Hodtani, "Copula-based analysis of physical layer security performances over correlated Rayleigh fading channels," *IEEE Trans. Inf. Forensics Secur.*, vol. 16, pp. 431–440, Aug. 2020.

[57] F. R. Ghadi *et al.*, "A Gaussian copula approach to the performance analysis of fluid antenna systems," *IEEE Trans. Wireless Commun.*, vol. 23, no. 11, pp. 17573–17585, Nov. 2024.

[58] M. Abramowitz and I. A. Stegun, *Handbook of mathematical functions*, 1972.

[59] M. Abramowitz and I. A. Stegun, *Handbook of mathematical functions with formulas, graphs, and mathematical tables*, vol. 55. US Government printing office, 1968.

[60] I. S. Gradshteyn and I. M. Ryzhik, *Table of integrals, series, and products*. Academic press, 2007.

[61] S. Al-Ahmadi and H. Yanikomeroglu, "On the approximation of the generalized-K distribution by a gamma distribution for modeling composite fading channels," *IEEE Trans. Wireless Commun.*, vol. 9, no. 2, pp. 706–713, Feb. 2010.